

Global biogenic isoprene emissions 2013-2020 inferred from satellite isoprene observations

Hui Li^{1,2#}, Philippe Ciais¹, Pramod Kumar¹, Didier A. Hauglustaine¹, Frédéric Chevallier¹, Grégoire Broquet¹, Dylan B. Millet³, Kelley C. Wells³, Jinghui Lian^{1,4}, Bo Zheng^{2,5}

¹Laboratoire des Sciences du Climat et de l'Environnement, LSCE/IPSL, CEA-CNRS-UVSQ, Université Paris-Saclay, F-91191 Gif-sur-Yvette, France.

²Shenzhen Key Laboratory of Ecological Remediation and Carbon Sequestration, Institute of Environment and Ecology, Tsinghua Shenzhen International Graduate School, Tsinghua University, Shenzhen 518055, China.

³University of Minnesota, St. Paul, MN 55108, USA.

⁴Origins.earth, SUEZ Group, Immeuble Altiplano, 4 Place de la Pyramide, 92800 Puteaux, France

⁵State Environmental Protection Key Laboratory of Sources and Control of Air Pollution Complex, Beijing 100084, China.

Correspondence to: Hui Li (hui.li@lsce.ipsl.fr)

Abstract. Isoprene, the most emitted biogenic volatile organic compound, exerts a remarkable influence on atmospheric oxidation capacity, air quality, and climate. Most existing top-down atmospheric estimates of isoprene emissions rely on observational formaldehyde (HCHO) as an indirect proxy, even though HCHO is produced from multiple precursors. Recent advances in satellite retrievals of isoprene concentrations from the Cross-track Infrared Sounder (CrIS) enable a direct constraint on isoprene emission inversions. Yet global, multi-year isoprene-based atmospheric inversions are still lacking. Here, we present global, monthly biogenic isoprene emission maps spanning 2013–2020, derived from a mass-balance inversion framework that assimilates CrIS-retrieved isoprene columns into the LMDZ-INCA chemistry–transport model. The global biogenic isoprene emissions average is of 456 ± 238 TgC yr⁻¹ over 2013–2020, which is broadly consistent with existing inventories and HCHO-based inversion estimates. The LMDZ-INCA simulations using this estimate of the emissions exhibit improved spatial agreement and reduced biases relative to two independent satellite HCHO retrieval products and to ground-based optical measurements, confirming the robustness of this inversion framework. The seasonal cycle of emissions is dominated by the Northern Hemisphere, driven by the strong seasonality in temperature and vegetation biomes. Interannually, emissions vary by on average 14 TgC yr⁻¹ (1-sigma standard deviation). Two major emission peaks are found in 2015–2016 (456 TgC yr⁻¹) and 2019–2020 (478 TgC yr⁻¹), coinciding with El Niño and widespread extreme heat-wave events, underscoring the dominant influence of temperature anomalies that increase biogenic emissions. Regional analyses identify the Amazon as the largest contributor to the interannual variability, accounting for 22.3% of the global interannual variance in isoprene emissions. Temperature emerges as the primary driver of regional interannual emissions, with its influence modulated by leaf area index and radiation to varying degrees across regions. As one of the earliest attempts at a global, multi-year inversion based on isoprene

observations, this dataset provides input for air quality and climate-chemistry models. The isoprene emission dataset is available at <https://doi.org/10.5281/zenodo.16214776> (Hui et al., 2025).

1. Introduction

Isoprene (2-methyl-1,3-butadiene, C_5H_8), the most abundantly emitted biogenic volatile organic compound (BVOC), accounts for 40%-60% of global BVOC emissions, with annual fluxes estimated between 350 and 600 TgC yr⁻¹, showing a considerable uncertainty (Sindelarova et al., 2022; Messina et al., 2016; Wang et al., 2024a). Its emissions are primarily regulated by land cover type, leaf area, climate conditions (e.g., temperature, radiation), and atmospheric CO₂ concentration. Among these, land cover, global warming, and rising CO₂ levels drive long-term emission trends, while extreme climate events govern short-term fluctuations. Emission factors (EFs), defined as the rate of emissions per unit area under standardized light and temperature conditions (Henrot et al., 2017), differ substantially among land cover types. Broadleaf trees exhibit the highest EFs, followed by needleleaf trees, shrubs, grasses, and crops in decreasing order (Opacka et al., 2021; Guenther et al., 2012). Recent studies further indicate that global warming can enhance isoprene emissions from shrubs and sedges, highlighting their emerging role in biogenic fluxes (Wang et al., 2024d; Wang et al., 2024b; Wang et al., 2024c). Of all climate variables, temperature is widely recognized as the primary driver (Seco et al., 2022; Stavrakou et al., 2018), yet the variability of its influence across regions is not well characterized. The role of CO₂ is nuanced: although CO₂ fertilization is estimated to have historically enhanced isoprene emissions, future increases in CO₂ concentrations may suppress emissions through physiological inhibition effects (Unger, 2013; Pacifico et al., 2012).

Once emitted, isoprene undergoes rapid atmospheric oxidation, primarily initiated by hydroxyl radicals (OH) (e.g., ~1 h at $[OH] = 5 \times 10^6$ molecules cm⁻³ at T=298 K) and by ozone (O₃) (Bates and Jacob, 2019). Due to its high reactivity, isoprene plays a pivotal role in tropospheric chemistry: it modulates the oxidative capacity of the atmosphere, influences the atmospheric lifetime of greenhouse gases such as methane (CH₄) (Pound et al., 2023; Zhao et al., 2025), and serves as a major precursor to secondary organic aerosols through condensational growth and new particle formation, which exacerbate regional air pollution (Xu et al., 2021; Curtius et al., 2024). Moreover, isoprene affects O₃ chemistry in a nonlinear manner—acting as a net source under high-NO_x conditions and a net sink in low-NO_x regimes (Geddes et al., 2022). A similar NO_x dependence is observed for formaldehyde (HCHO) yields from isoprene, where elevated NO_x levels accelerate production rates and increase the overall HCHO yield (Wolfe et al., 2016).

Accurately quantifying isoprene emissions is essential for improving air quality forecasts and climate-chemistry model predictions. Two commonly adopted approaches are bottom-up models and top-down atmospheric inversions. Among bottom-up models, the Model of Emissions of Gases and Aerosols from Nature (MEGAN) is the most widely used. It parameterizes isoprene emissions as a function of climate drivers such as light, temperature, and biological variables leaf area index (LAI) and phenology (Guenther et al., 2012). Variability across inventories reflects both differences in parameterizing functional relationships

with climate drivers and, more importantly, inconsistencies in representing vegetation distributions, land-use changes, and EFs (Do et al., 2025; Messina et al., 2016). While improvements are ongoing, bottom-up estimates remain highly uncertain due to unclear EFs especially over tropical regions, structural limitations, and the complex physiological responses of plants to meteorological variability (Cao et al., 2021). Top-down inversion methods offer a complementary strategy by deriving emissions with atmospheric observations. Most existing inversions rely on satellite-retrieved HCHO, a major oxidation product of isoprene, and exploit the relationship between HCHO concentrations and isoprene fluxes (Millet et al., 2008; Barkley et al., 2013; Marais et al., 2012). However, HCHO-based inversions face inherent limitations, including the non-linear nature of isoprene–OH chemistry (Valin et al., 2016) which is also a challenge for isoprene-based inversions, uncertainties in NO_x-dependent HCHO yields, smearing effects causing spatial displacement between isoprene emissions and HCHO formation (Wolfe et al., 2016), and contributions from non-isoprene HCHO precursors such as CH₄ and other volatile organic compounds (Nussbaumer et al., 2021).

Direct atmospheric inversion assimilating isoprene concentrations provides a promising alternative to HCHO-based approaches, partly circumventing those limitations. Historically, this strategy was limited by the lack of atmospheric isoprene observations. Recent advances in infrared remote sensing now enable global retrievals of isoprene concentrations from satellites such as the Cross-track Infrared Sounder (CrIS) (Fu et al., 2019; Palmer et al., 2022; Wells et al., 2022), offering new opportunities for direct inversion. To date, however, isoprene-based inversions remain limited; to our knowledge, only a few studies have been conducted at the regional scale, focusing on areas such as the Amazon Basin, Asia, etc. (Sun et al., 2025; Wells et al., 2020; Choi et al., 2025). No global, multi-year continuous isoprene-based atmospheric inversion has been reported yet.

To fill this gap, we present a global, eight-year (2013–2020), monthly biogenic isoprene emission inversion, based on CrIS-retrieved isoprene concentrations derived through an artificial neural network (ANN) approach (Wells et al., 2020; Wells et al., 2022) and assimilated into the LMDZ-INCA 3D chemistry–transport model. This framework provides a direct top-down constraint on isoprene emissions, complementing traditional HCHO-based approaches and enabling the first global, multi-year assessment of isoprene fluxes. The inferred emissions capture key spatiotemporal patterns, including pronounced seasonal cycles dominated by the Northern Hemisphere and two major emission peaks in 2015–2016 and 2019–2020 linked to strong temperature anomalies. These advances highlight the sensitivity of biogenic emissions to temperature variability and demonstrate the potential of CrIS-based inversions to improve emission estimates. The resulting dataset provides a valuable resource for air quality forecasting and climate modeling, and offers valuable insights into biosphere–atmosphere interactions under changing environmental conditions.

2. Methods

2.1 Observations of isoprene and HCHO

This study employs three satellite datasets, CrIS isoprene, TROPOMI HCHO, and OMPS HCHO, along with ground-based HCHO column observations from the Pandonia Global Network (PGN), to derive and evaluate biogenic isoprene emissions. CrIS, a Fourier transform spectrometer aboard the Suomi National Polar-orbiting Partnership (Suomi-NPP) launched on 28 October 2011, provides daily global observations around 13:30 local time (Han et al., 2013). We use global monthly-mean CrIS isoprene column concentrations from January 2013 to December 2020 (resolution of 0.5° latitude \times 0.625° longitude), retrieved using an ANN approach that links spectral indices from CrIS radiances to isoprene columns based on a training dataset constructed from an ensemble of randomized chemical transport model profiles (Wells et al., 2020; Wells et al., 2022). As the ANN retrieval does not include scene-specific vertical sensitivity information, the CrIS-retrieved isoprene columns are directly compared with model-simulated columns. It is noteworthy that CrIS retrievals lack coverage in high-latitude regions north of 60°N (Fig. S1), where the inversion retains their prior emission in this study.

Two independent satellite-based datasets of HCHO column concentrations, OMPS-NM and TROPOMI, are used to indirectly evaluate the posterior-simulated HCHO columns. The instrument OMPS-NM, flown with CrIS on Suomi-NPP, measures backscattered solar radiation in the 300–380 nm range at $\sim 13:30$ local time, delivering near-global coverage with a spatial resolution of $50\text{ km} \times 50\text{ km}$ (Abad, 2022; Nowlan et al., 2023). We use its OMPS_NPP_NMHCHO_L2 retrieval dataset, applying standard quality filters: `main_data_quality_flag` = 0, solar zenith angle (SZA) $< 70^\circ$, and cloud fraction < 0.4 . TROPOMI, a nadir-viewing hyperspectral spectrometer aboard the European Sentinel-5 Precursor satellite launched in October 2017, provides global HCHO column densities at a similar overpass time ($\sim 13:30$ local time), with finer spatial resolution ($7\text{ km} \times 3.5\text{ km}$ prior to August 2019 and $5.5\text{ km} \times 3.5\text{ km}$ thereafter). We use the TROPOMI level 2 product (TROPOMI-RPRO-v2.4), filtered by `qa_value` ≥ 0.75 (ESA, 2020). To ensure comparability with the satellite retrievals in evaluation, modeled HCHO concentrations from LMDZ-INCA are first processed with the averaging kernels (AK) provided with the two satellite HCHO products to generate respective model-equivalent columns, and then resampled to the satellite overpass times ($\sim 13:30$ local time). All satellite datasets are regridded to a common spatial resolution of 1.27° latitude \times 2.5° longitude for consistency. The annual spatial distribution of the three satellite datasets over the globe is shown in Fig. S1.

In addition to satellite data, we also incorporate ground-observed HCHO columns from the PGN network (<https://www.pandonia-global-network.org/>) for independent evaluation of the posterior simulation of HCHO concentrations. Considering data availability and consistency across all three HCHO datasets, we select the year 2019 as a representative period for the posterior evaluation (Section 3.1).

2.2 LMDZ-INCA global chemistry-transport model

To establish the relationship between isoprene emissions and atmospheric concentrations, we use the LMDZ-INCA global chemistry–aerosol transport model (Hauglustaine et al., 2004). The model is coupled with the ORCHIDEE (Organizing Carbon and Hydrology in Dynamic Ecosystem) land surface model, which

dynamically simulates vegetation processes and provides prior estimates of biogenic isoprene emissions using the following formulation (Messina et al., 2016):

$$F = \text{LAI} \times \text{SLW} \times \text{EFs} \times \text{CTL} \times L \quad (1)$$

where LAI is the leaf area index, SLW is the specific leaf weight, EFs denotes the base emissions at the leaf level for a Plant Functional Type (PFT) at standard conditions of temperature ($T=303.15 \text{ K}$) and photosynthetically active radiation ($\text{PAR}=1000 \mu\text{mol m}^{-2} \text{ s}^{-1}$), CTL is the emission activity factor representing environmental responses (e.g., to temperature and light), and L accounts for leaf age-dependent modulation of emissions. A detailed description of the ORCHIDEE-based isoprene emission (global emissions: $\sim 512 \text{ TgC yr}^{-1}$) scheme can be found in Messina et al. (2016). In addition to isoprene, ORCHIDEE also simulates emissions of other BVOC, including monoterpenes, methanol, acetone, sesquiterpenes, and others. A detailed comparison between ORCHIDEE- and MEGAN-simulated BVOC emissions is provided in Messina et al. (2016).

LMDZ-INCA contains a state-of-the-art $\text{CH}_4\text{--NO}_x\text{--CO--NMHC--O}_3$ tropospheric photochemistry scheme with a total of 174 tracers, including the chemical degradation scheme of 10 non-methane hydrocarbons (NMHCs): C_2H_6 , C_3H_8 , C_2H_4 , C_3H_6 , C_2H_2 , a lumped $\text{C}>4$ alkane, a lumped $\text{C}>4$ alkene, a lumped aromatic, isoprene and α -pinene. The mechanism comprises 398 homogeneous, 84 photolytic, and 33 heterogeneous reactions, and is continuously updated to integrate newly identified chemical processes and reaction pathways, thereby improving the representation of atmospheric composition and oxidation capacity (Hauglustaine et al., 2004; Folberth et al., 2006; Pletzer et al., 2022; Sand et al., 2023; Terrenoire et al., 2022; Novelli et al., 2020; Wennberg et al., 2018). Reactions directly related to isoprene and HCHO are listed in Tables S1-S2.

Global LMDz-INCA simulations are performed at a horizontal resolution of 1.27° latitude \times 2.5° longitude, with 79 vertical hybrid sigma-pressure levels extending up to $\sim 80 \text{ km}$, and are nudged to ERA5 wind fields. Turbulent mixing within the planetary boundary layer (PBL) is parameterized following Mellor and Yamada (1982) scheme while thermal convection is represented using the Tiedtke (1989) convection parameterization. The vertical profiles of LMDZ-INCA simulated isoprene and HCHO concentrations over Amazon region (Fig. S2) show a continuous decrease from the surface upward, consistent with previous studies (Fu et al., 2019; Hewson et al., 2015). Monthly global anthropogenic emissions of chemical species and gases are taken from the open-source Community Emissions Data System (CEDS) gridded inventories, wherein NO_x emissions include eleven anthropogenic sectors and fertilizer-related soil sources, with global totals of around 113 Tg yr^{-1} (Hoesly et al., 2018; McDuffie et al., 2020). Fire emissions are taken from the Global Fire Emissions Database version 4 (GFED4) (Van Der Werf et al., 2017). For isoprene, monthly mean emissions from the input files are redistributed diurnally based on the local solar zenith angle to account for their strong photochemical dependence. Further details of the LMDZ-INCA configuration are provided by Kumar et al. (2025). A three-year spin-up simulation (2010–2012) is conducted to equilibrate the system, followed by a base simulation for 2013–2020. During the base simulation, isoprene and HCHO concentrations and isoprene emissions are sampled hourly. These hourly outputs are then used for model–observation comparisons and for performing the global inversion of isoprene emissions over the 2013–2020 period.

2.3 Inversion methodology

In order to assimilate CrIS isoprene retrievals into the LMDZ-INCA model, we apply the finite-difference mass balance (FDMB) inversion framework (Cooper et al., 2017). Given isoprene's short atmospheric lifetime, typically a few hours (~ 3 h at $[\text{OH}] = 1 \times 10^6$ molecules cm^{-3} at $T=298$ K) (Bates and Jacob, 2019; Fu et al., 2019), its horizontal transport is generally limited to a few tens of kilometers, supporting the assumption of a local relationship between emissions and column concentrations. Although this assumption may break down at high latitudes near the poles, its impact is negligible as isoprene emissions are largely confined to 60°S – 60°N . In addition, in tropical regions with low NO_x , isoprene-driven OH suppression can prolong its lifetime and potentially violate the local linearity assumption (Wells et al., 2020). A detailed discussion of NO_x effects is provided in Section 2.4. The final biogenic emissions for each model grid cell and month are calculated as follows:

$$E_{\text{posterior},i,m} = E_{\text{prior},i,m} \left(1 + \beta_{i,m} \frac{\Omega_{\text{obs},i,m} - \Omega_{\text{simu},i,m}}{\Omega_{\text{simu},i,m}} \right) \quad (2)$$

In Eq. (2), i denotes the model grid cell in the $1.27^\circ \times 2.5^\circ$ mesh, m indicates the month, and $\Omega_{\text{obs},i,m}$ and $\Omega_{\text{simu},i,m}$ represent the observed and simulated monthly mean isoprene column concentrations (molecules cm^{-2}), respectively. To account for the strong diurnal variability of the isoprene column, $\Omega_{\text{simu},i,m}$ only considers the CrIS overpass time ($\sim 13:30$ local time) in its average, for consistency with $\Omega_{\text{obs},i,m}$. $E_{\text{posterior},i,m}$ and $E_{\text{prior},i,m}$ refer to the posterior and prior isoprene emissions ($\text{kgC m}^{-2} \text{s}^{-1}$), respectively. $\beta_{i,m}$ is a dimensionless factor representing the local relative response of modeled isoprene columns ($\Delta\Omega_{\text{simu}}/\Omega_{\text{simu}}$) to relative changes in prior emissions ($\Delta E_{\text{prior}}/E_{\text{prior}}$) as calculated below:

$$\beta_{i,m} = \frac{\Delta E_{\text{prior},i,m} / E_{\text{prior},i,m}}{\Delta \Omega_{\text{simu},i,m} / \Omega_{\text{simu},i,m}} \quad (3)$$

To derive $\beta_{i,m}$, we conduct two LMDZ-INCA simulations each year: one using the original ORCHIDEE-based prior isoprene emissions, and the other with those emissions uniformly reduced by 40% (based on the difference between simulated and observational isoprene columns). Sensitivity tests using alternative perturbations (+25%) confirm that $\beta_{i,m}$ is overall insensitive to the choice of perturbation magnitude, with global mean differences around -10% (average $(\beta_{+25\%}/\beta_{-40\%})$ ratio=0.9; Fig. S3). The robustness of β is further discussed in Section 2.4. To avoid extreme changes, we keep $\beta_{i,m}$ within the range 0-10, and the inversion is performed only over land grid cells. An illustration of the spatial distribution of monthly mean β values for 2019 is shown in Fig. S4, with a global annual mean of approximately 0.85. Lower β values (around 0.6-0.7) are generally found over tropical hotspots such as the Amazon, while higher values (≥ 1) are found across much of the Northern Hemisphere, similar to previous studies (Wells et al., 2020). In this study, Posterior updates are only applied to grid cells with valid β and CrIS observations, while emissions in the remaining grids are retained at their prior values. During 2013–2020, an average of 67.6% of land grid cells are updated per month, representing 99.0% of prior monthly emissions (Fig. S5), since missing data are concentrated in

high-latitude regions with low emissions. For a clearer regional analysis, we divide the globe into 15 regions, as listed in Table 1 and shown in Fig. S6.

Table 1. Regional classification in this study, with classified map presented in Fig. S6.

Abbreviations	Full names
AMZ	Amazon
RSAM	Rest of Southern America (other than Amazon)
EQAF	Equatorial Africa
NAF	Northern Africa
SEAS	Southeast Asia
CHN+KAJ	China+Korea+Japan
SAS	South Asia
SAF	Southern Africa
USA	The United States
MIDE	Mideast
OCE	Oceania
RUS+CAS	Russia+Central Asia
CAM	Central America
EU	Europe
CAN	Canada

2.4 The robustness of the linear relationship between isoprene concentrations and emissions

A central assumption in our FDMB inversion framework is the linear response of isoprene concentrations to changes in emissions within certain perturbations. To assess the robustness of this assumption, we identified grids where the β difference between the +25% and -40% perturbations is within $\pm 20\%$ (i.e., $\beta_{+25\%}/\beta_{-40\%}$ ratio between 0.8 and 1.2 in Fig. S3). These grids account for 70.8% of global isoprene emissions, indicating that the linearization approximately holds across most emissions in this study. The grid-scale statistics of $\beta_{+25\%}/\beta_{-40\%}$ shows that the average ratio falls within 0.86-0.90, and median value within 0.85-89 each month (Fig. S7). The remaining deviations, primarily located in low-isoprene environments (Fig. S8), point to localized nonlinear responses, yet the overall relationship between isoprene emissions and its concentrations can be considered approximately linear at the grid scale within the range of perturbations and corrections of the inversions. It is important to note, however, that the perturbation range (-40% to +25%) represents a substantial 65% change in emissions, which may generate large deviations from linearity. In fact, emission variations are typically moderate; in this study, more than 63% of the grid cells exhibit posterior-prior differences within 65%, accounting for over 82% of the global total emissions on average, suggesting that β is relatively insensitive to the magnitude of emission perturbations in most regions (Fig. S9).

To further asses the linearization, we take 2019 as an example year to apply the iterative finite difference mass balance method following the approach of Cooper et al. (2017). After the initial inversion with a -40% perturbation, subsequent iterations use a smaller -10% perturbation, as the first step already reduces the model-observation bias substantially. The inversion is repeated using the updated emissions until convergence, with the final solution obtained when the average model-observation differences across the 15

regions change by less than 5%. Convergence is achieved after four iterations. The comparison between the single-step and four-iteration results shows that the global annual total emissions differ by about 5.3%, while the largest regional difference occurs in Mideast (MIDE) at about -20% (Fig. S10). The iterative procedure effectively reduces model–observation discrepancies, confirming the optimization capability of the inversion system. However, given the relatively small difference from the single-step inversion and the high computational cost, the single-step approach is considered sufficient for the long-term emission dynamics analysis in this study.

Another sensitivity test excludes low-isoprene regions (two tests excluding grids with monthly mean columns $<0.5 \times 10^{15}$ molec cm⁻² or $<1 \times 10^{15}$ molec cm⁻²) from the inversion by keeping the prior unchanged, ensuring that optimization occurs only where the linearization of the emission–concentration relationship is robust. The resulting posterior shows minimal impact on global totals, with an annual difference of less than 9% compared to the base inversion, and the largest regional deviation of about 40% occurring in Northern Africa (NAF) and MIDE (Fig. S11). These results confirm that low-isoprene regions indeed contribute higher uncertainties during optimization, consistent with the uncertainty assessment in Section 3.2. Nevertheless, the interannual variability derived under this configuration remains consistent with that from the full inversion, indicating that despite these uncertainties, the long-term emission dynamics identified in this study are robust (Fig. S11).

2.5 The impact of NO_x concentration on inversion

The linearity between isoprene concentrations and emission changes is strongly modulated by ambient NO_x levels and by isoprene itself because both species directly influence the oxidative capacity of the atmosphere and, consequently, the chemical lifetime of isoprene (Wennberg et al., 2018). Under high-NO_x conditions, isoprene oxidation proceeds efficiently due to rapid OH radical recycling, supporting a robust linear relationship between concentrations and emissions. In contrast, in low-NO_x environments, the reduced atmospheric oxidizing capacity prolongs the chemical lifetime of isoprene, leading to a superlinear response where concentrations increase disproportionately with emissions (Fu et al., 2019; Wells et al., 2020). This nonlinearity reduces the validity of the linear assumption in regions with low NO_x, necessitating a careful evaluation of β non-linearity and sensitivity to ambient NO_x levels.

In the LMDZ-INCA simulations, NO_x emissions are prescribed from the CEDS global inventories (McDuffie et al., 2020), which cover eleven anthropogenic sectors, including agriculture, energy production, transportation (on-road and non-road), residential, commercial, and international shipping, as well as soil NO_x emissions from synthetic and manure fertilizers. Detailed configurations are provided in Kumar et al. (2025). Compared to TROPOMI-retrieved NO₂ tropospheric columns from the TROPOMI-RPRO-v2.4 product, LMDZ-INCA simulates an overall negative bias, with NO₂ concentrations approximately 30% lower than observed (Figs. S12–S13). This underestimation of NO₂ leads to an overestimation of isoprene lifetime and, consequently, a systematic underestimation of β in Eq. (3). The effect is particularly pronounced in regions with high isoprene concentrations, consistent with the ~10% reduction of β observed in the +25%

isoprene emission perturbation test (Fig. S2). To further assess the influence of NO_x conditions on the inversion, we perform a sensitivity test using +25% NO_x emissions for 2019. The results show negligible differences from the base inversion, with a global annual total deviation of less than 0.1% and the largest regional difference of 0.9% over South Asia (SAS) (Fig. S14).

2.6 The impact of prior choice on inferred isoprene emissions

To evaluate the sensitivity of the inversion to the choice of prior emissions, two additional sensitivity experiments are conducted using MEGAN-MACC (Sindelarova et al., 2014) and MEGAN-ERA5 (also known as CAMS-GLOB-BIOv3.1) (Sindelarova, 2021; Sindelarova et al., 2022) isoprene inventories, both of which are mechanistically distinct from the ORCHIDEE-based prior employed in the main analysis. The inversions are performed for the year 2019 following the same setup and observational constraints. Results show that the inferred global total isoprene emissions differ by less than 3.5% among the three prior configurations: deviations between the MEGAN-MACC-based inversion (500 Tg yr⁻¹) and our posterior global total (485 Tg yr⁻¹) are 3.1%, while those between the MEGAN-ERA5-based inversion (495 Tg yr⁻¹) and our posterior are 2.1%, suggesting that the inversion framework remains robust to the choice of prior in global annual totals (Fig. S15). From a regional perspective, the largest differences occur in Oceania, where posterior emissions derived from MEGAN-MACC and MEGAN-ERA5 differ from our reference posterior by 60.6% and 17.4%, respectively (Fig. S16). Although Oceania shows the largest posterior discrepancies globally, these differences are substantially smaller than those in their priors (19 Tg yr⁻¹ in ORCHIDEE, 108 Tg yr⁻¹ in MEGAN-MACC, and 61 Tg yr⁻¹ in MEGAN-ERA5 in 2019), indicating that the inversion effectively reconciles regional inconsistencies and converges toward observational constraints even where prior emissions diverge markedly. Overall, these tests demonstrate that the optimized emissions are primarily driven by observational constraints rather than by the characteristics of the prior inventory.

3. Results

3.1 Evaluation of the posterior simulation of HCHO and isoprene

As shown in Fig. 1, the posterior simulation improves over prior results, both in terms of spatial distribution and correlation with observations. For HCHO, model grid-level comparison against TROPOMI retrievals shows that the global Root Mean Squared Error (RMSE) decreases from 0.29×10^{16} to 0.18×10^{16} molecules cm⁻², reflecting a substantial improvement in model–observation agreement relative to the prior simulation. Similar improvements are seen when compared with OMPS HCHO retrievals (Fig. S17), indirectly supporting the reliability of the posterior emissions. This enhancement is particularly pronounced over the Amazon, where the RMSE decreases by 0.31×10^{16} molecules cm⁻² (Fig. S18). For isoprene, the model–observation agreement improves more substantially, validating the linearization of LMDZ-INCA based on a perturbation and the assumed local relationship between emissions and column concentrations. The regression slope between posterior simulations and CrIS observations decreases from 2.61 to 1.07, while

RMSE reduces from 5.69×10^{15} to 1.22×10^{15} molecules cm^{-2} . Biases in key tropical regions such as the Amazon are notably reduced, with regional RMSE of isoprene decreasing by 19.59×10^{15} molecules cm^{-2} (Fig. S18). In addition to satellite comparisons, posterior-simulated HCHO also shows a modest improvement in agreement with ground-based HCHO column concentrations from the PGN network, with the RMSE decreasing from 0.45×10^{16} to 0.42×10^{16} molecules cm^{-2} (Fig. S19). In 2020, when more PGN sites became available (increasing from 15 in 2019 to 20), the posterior HCHO concentrations also better match the PGN observations, with the RMSE decreasing from 0.49×10^{16} to 0.47×10^{16} molecules cm^{-2} (Fig. S19). These improvements relative to various HCHO observations consistently demonstrate the ability of the inversion framework to derive reliable estimates of the isoprene emissions and enhance model performance across diverse observational benchmarks.

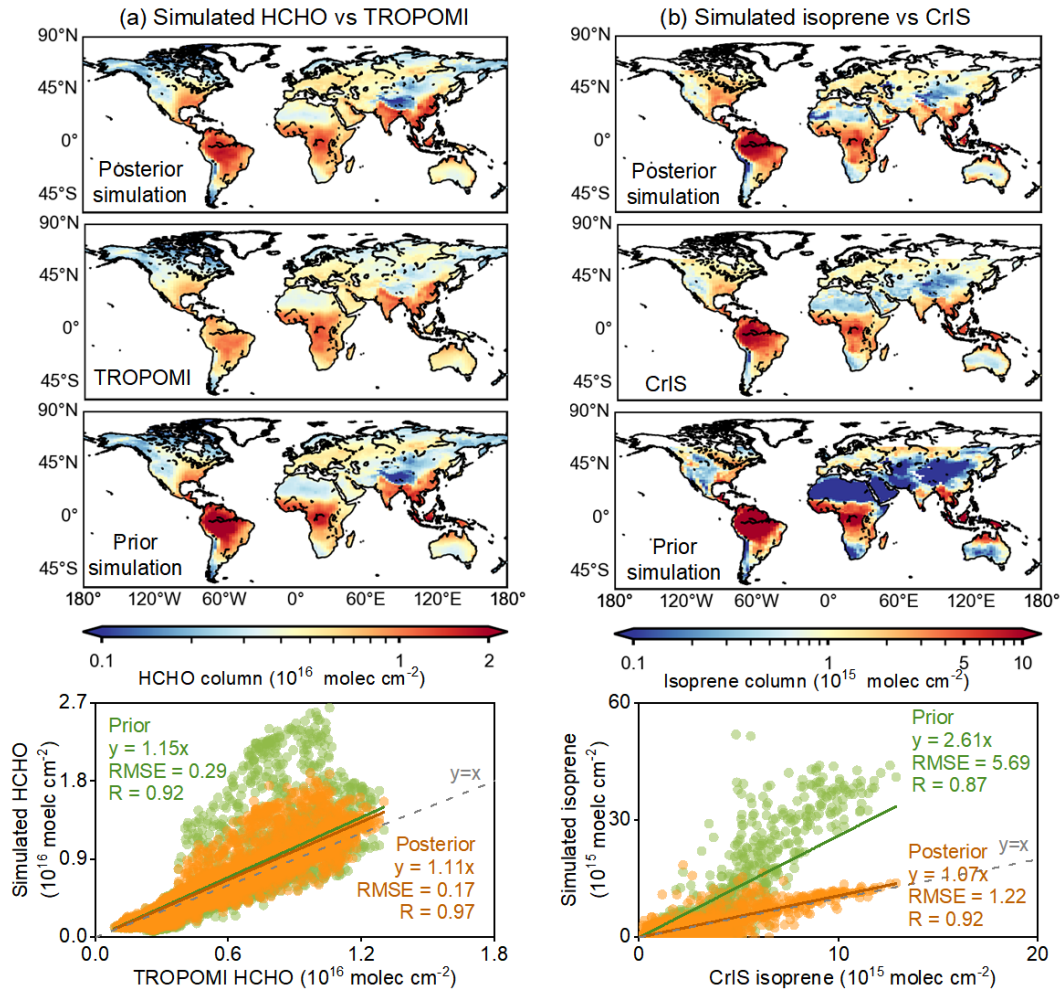


Figure 1. Evaluation of the posterior LMDZ-INCA simulation using TROPOMI HCHO and CrIS isoprene observations in 2019. (a) and (b) present the comparison of the simulated HCHO with TROPOMI observations, and of the simulated isoprene with CrIS observations, respectively. From top to bottom: the global distribution of model grid-scale annual mean of the posterior simulation, satellite observation (from TROPOMI in (a) column and from CrIS in (b) column), prior simulation of the column concentrations, and correlation between annual-mean simulation and observation across the model grid-cells covered by the observation.

3.2 Uncertainty estimation

In the FDMB inversion framework, posterior uncertainty (σ_p) is analytically estimated by minimizing the mass balance cost function, following the formulation of Cooper et al. (2017). It is important to note, however, that σ_p does not account for potential structural errors in the LMDZ-INCA model, such as uncertainties in chemical mechanisms or meteorological fields. This limitation highlights the importance of independently evaluating the posterior estimates against external datasets to assess the robustness and reliability of the inferred emissions (seen in Section 3.1).

$$\frac{1}{\sigma_p^2} = \frac{1}{\sigma_a^2} + \frac{1}{\sigma_e^2} \quad (4)$$

where σ_a and σ_e represent the relative uncertainties in prior emissions and in the gridded monthly satellite observations, respectively. The prior emissions used in this study are derived from ORCHIDEE, a bottom-up, process-based model. Its uncertainties stem from factors including LAI, SLW, EFs, CTL, and L (as shown in Eq. 1). PFT-dependent EFs vary substantially across different emission inventories, assigned a high uncertainty of 100% (Do et al., 2025; Weber et al., 2023). Among the remaining factors, LAI and the light-dependent fraction (LDF) that controls the CTL term are especially influential. According to Messina et al. (2016), the relative difference in LAI between the ORCHIDEE model and MODIS observations is approximately 50%. Therefore, we assign a 50% uncertainty to LAI, while a 20% uncertainty is applied to the remaining parameters. Applying standard error propagation for multiplicative variables yields a combined prior uncertainty (σ_a) of 117.0%, which represents a rough estimation of the overall uncertainty:

$$\sigma_a = \sqrt{\sigma_{\text{LAI}}^2 + \sigma_{\text{SLW}}^2 + \sigma_{\text{EFs}}^2 + \sigma_{\text{LDF}}^2 + \sigma_L^2} \quad (5)$$

The CrIS isoprene retrievals used in this study are based on an ANN retrieval approach. Retrieval uncertainties are spatially variable, depending on the column concentrations. According to Wells et al. (2022), retrieval uncertainties are generally <25% over high-concentration area ($\geq 10 \times 10^{15}$ molec cm⁻²), and >50% in low-concentration area ($< 2 \times 10^{15}$ molec cm⁻²). To account for this, we apply a piecewise uncertainty function for σ_e based on the observed isoprene column in each grid cell. An additional 20% uncertainty is applied to account for potential systematic effects, informed by the discrepancies observed in independent dataset comparisons (Wells et al., 2022). Here we assume these two uncertainty components (random retrieval error and systematic error) to be independent and additive in a simplified linear formulation, such that the final observational uncertainty is set at 45% for grid cells with $\Omega_{\text{obs}} \geq 10 \times 10^{15}$ molec cm⁻², varies linearly between 45% and 70% for $2 \times 10^{15} \text{ molec cm}^{-2} < \Omega_{\text{obs}} < 10 \times 10^{15} \text{ molec cm}^{-2}$, and the same linear relation is extrapolated to $\Omega_{\text{obs}} < 2 \times 10^{15} \text{ molec cm}^{-2}$ with an upper cap of 100%. Grid cells without valid observations remain at their prior values, and their posterior uncertainties are therefore set equal to the prior uncertainties. Prior and observational uncertainties are then combined using Eq. (4), and the resulting cell-level posterior relative uncertainties are aggregated to the global scale through area-weighted averaging. Taking 2020 as an example, the spatial distribution of cell-level posterior uncertainties is shown in Fig. 2, with the uncertainty for global annual isoprene emissions estimated at 51.6%.

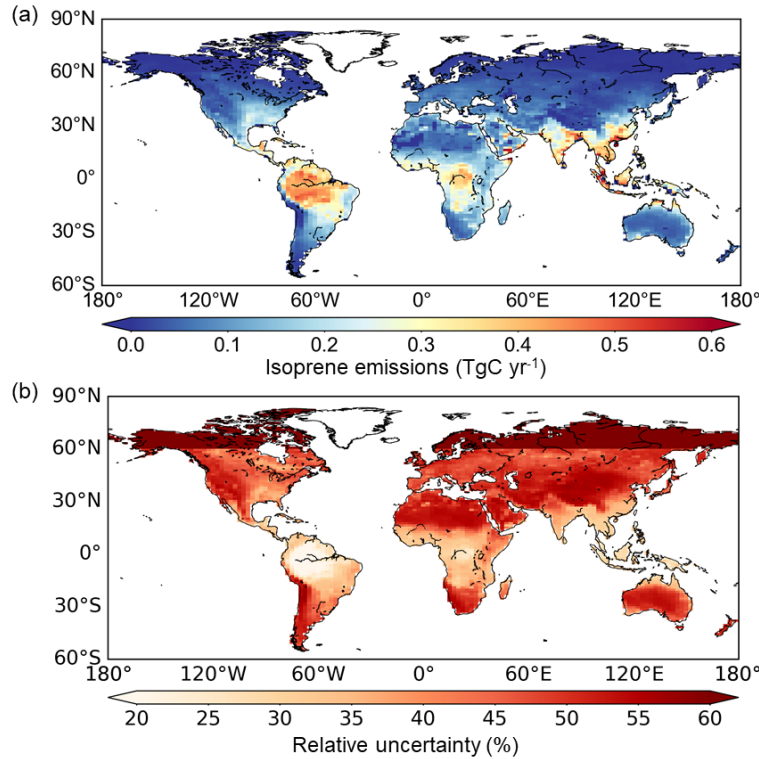


Figure 2. (a) Global distribution of isoprene emissions (TgC per grid cell of 1.27° latitude \times 2.5° longitude per year) and (b) relative uncertainties (%) in 2020. The uncertainties of global totals are area-weighted averages.

3.3 Seasonal pattern of isoprene emissions

Seasonally, the posterior emissions exhibit a pronounced peak during July–September (JAS), and a minimum in December, January, and February (DJF) (Fig. 3). Over the study period (2013–2020), the global mean monthly isoprene emission is approximately 38 TgC month⁻¹, rising by 42% to 54 TgC month⁻¹ during JAS and declining sharply by 34% to 25 TgC month⁻¹ during DJF. This seasonal cycle agrees with recent HCHO-based inversion results (Müller et al., 2024) but differs markedly from that in current bottom-up inventories: MEGAN-MACC (Sindelarova et al., 2014) and MEGAN-ERA5 (also known as CAMS-GLOB-BIOv3.1) (Sindelarova, 2021; Sindelarova et al., 2022) (Figs. 3 and S20). The discrepancy primarily stems from an overestimation of isoprene emissions from Oceania (OCE) in current inventories. OCE contributes up to 92 TgC yr⁻¹ in MEGAN-MACC and 52 TgC yr⁻¹ in MEGAN-ERA5, exceeding half of the corresponding emissions from the Amazon (AMZ, 103 and 94 TgC yr⁻¹, respectively), and exhibits substantial seasonal variability (Fig. S21). Previous studies have attributed this likely overestimation of emissions and its seasonality over OCE to the parameterization of temperature and radiation responses, along with the use of high emission factors in bottom-up models (Emmerson et al., 2016; Emmerson et al., 2018). When OCE is excluded, both MEGAN inventories show a JAS peak and DJF minimum, exhibiting a broadly similar seasonal pattern to our posteriors (Fig. S22). Besides, sensitivity inversions using MEGAN-MACC and MEGAN-ERA5 as priors also reproduce a JAS maximum and DJF minimum, reversing the original prior seasonality. The posterior seasonality derived from all three priors aligns with that observed in CrIS isoprene

and OMPS HCHO concentrations (Fig. S20), indicating that the retrieved temporal variability reflects the observed atmospheric signals and demonstrating the robustness of the inferred seasonal cycle. The monthly variability in global isoprene emissions is largely driven by the Northern Hemisphere, mirroring strong seasonal fluctuations in temperature (correlation coefficients, $R=0.92$) and vegetation activity (R with $LAI=0.89$) (Figs. 3 and S23; Table S3). While these process relationships are inherently non-linear, correlation analysis provides a useful first-order approximation of regional responses and sensitivities. During JAS, Northern Hemisphere emissions peak at $41 \text{ TgC month}^{-1}$ and decline to $10 \text{ TgC month}^{-1}$ in DJF, accounting for nearly $\sim 100\%$ of the global JAS–DJF peak-to-trough difference ($\sim 30 \text{ TgC}$). In contrast, Southern Hemisphere emissions remain seasonally stable, averaging $14 \text{ TgC month}^{-1}$ during both JAS and DJF with negligible difference. This strong hemispheric asymmetry underscores the dominant role of the Northern Hemisphere in shaping the global seasonal cycle. Notably, the synchronicity between monthly emissions and temperature is stronger in the Northern Hemisphere ($R=0.96$) than in the Southern Hemisphere ($R=0.54$), reflecting the greater extent of mid-latitude land areas and sharper temperature seasonality in the north (Figs. 3b–3c, and S24). Additionally, stronger LAI variations in the Northern Hemisphere further reinforce this seasonal pattern (Figs. S25–S26) (Ren et al., 2024; Ma et al., 2023).

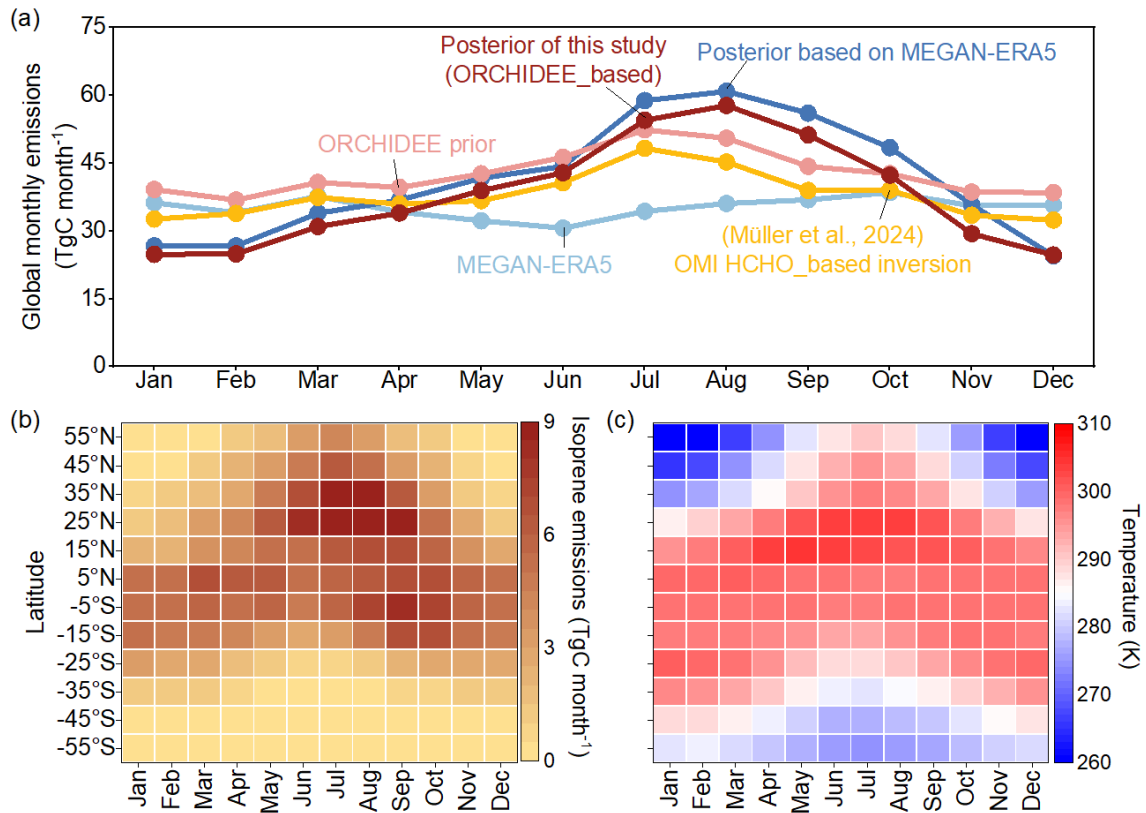


Figure 3. Monthly mean isoprene emissions from 2013 to 2020. (a) shows the global monthly pattern of ORCHIDEE prior and our posterior in this study, MEGAN-ERA5 (also known as CAMS-GLOB-BIOv3.1) inventory (Sindelarova, 2021) and posterior based on MEGAN-ERA5, as well as OMI HCHO-based isoprene inversion result (Müller et al., 2024). MEGAN-ERA5 is based on MEGAN v2.1, updated with ERA5 meteorology and CLM4 land cover (Sindelarova et al., 2022). (b)-(c) display monthly distributions of our estimated isoprene emissions (TgC) and temperature (K) by every 10° latitude band, respectively. We here only present the latitude range from 60°S to 60°N where emissions dominate ($\sim 99\%$). Temperature is acquired from ERA5. The monthly distributions of two MEGAN inventories

(MEGAN-MACC and MEGAN-ERA5), precipitation from ERA5, and the Leaf area index (LAI) from Pu et al. (2024) are presented in Fig. S25.

3.4 Interannual variation of global isoprene emissions

Over the study period (2013–2020), our global annual isoprene emissions average 456 ± 238 TgC yr⁻¹, falling within the range of existing bottom-up inventories and satellite-based inversion estimates (Fig. 4; Tables S2–S3). This value aligns closely with the MEGAN-ERA5 inventory (422 TgC yr⁻¹), whereas MEGAN-MACC reports a notably higher estimate of 573 TgC yr⁻¹, reflecting a positive bias relative to both our results and other datasets. Such overestimations in earlier MEGAN versions have been documented at global (Bauwens et al., 2016) and regional scales (Kaiser et al., 2018; Gomes Alves et al., 2023).

In terms of interannual variability, global annual isoprene emissions exhibit a standard deviation (1σ) of 14 TgC yr⁻¹ over 2013–2020, corresponding to a coefficient of variation of 3.1%. Despite differences in absolute magnitudes, the year-to-year variability simulated by both MEGAN inventories remains broadly consistent with our inversion-based estimates ($R=0.62$ – 0.64 for annual emission rates). This temporal coherence underscores the robustness of our posterior in capturing interannual variability. The spatial distribution of interannual variability is highly uneven, with tropical regions such as the AMZ, Equatorial Africa (EQAF), and SAS acting as the principal contributors. These regions show relatively large interannual standard deviations (2–3 TgC yr⁻¹, coefficient of variation: 3.3%–7.6%), primarily due to their status as global isoprene emission hotspots (Fig. 4b). On average, AMZ, EQAF, and SAS account for 15.5%, 11.5%, and 6.7% of global isoprene emissions, with corresponding emission intensities of 10, 6, and 6 gC m⁻² yr⁻¹, respectively (Fig. 4c).

A positive and a negative anomaly are observed in the interannual variation of global isoprene emissions, associated with the 2019–2020 extreme heat event and post-El Niño cooling in 2017, respectively, highlighting temperature as the primary driver of year-to-year variability. During 2019–2020, annual emissions averaged 478 TgC yr⁻¹, 1.5σ above the 2013–2020 mean (456 TgC yr⁻¹), with 2019 alone reaching 485 TgC yr⁻¹ (2σ above the mean) (Fig. S27). This peak coincides with widespread extreme heat (Robinson et al., 2021), with elevated temperatures observed across most regions, except for certain arid and semi-arid tropical zones such as NAF, SAS, and MIDE (Fig. S28). In contrast, emissions dipped to a minimum of 435 TgC yr⁻¹ in 2017 (1.5σ below the mean), with a cooling following the extreme 2015–2016 El Niño event, the most intense since 1950 (Hu and Fedorov, 2017). Although partially masked by the subsequent 2019–2020 peak, the 2015–2016 El Niño also triggered an earlier emission enhancement, with global emissions averaging 456 TgC yr⁻¹, exceeding the 2013–2018 baseline mean of 449 TgC yr⁻¹ (Fig. S27). During this period, most regions except OCE experienced substantial warming, surpassed only by the more extreme heat of 2019–2020 (Fig. S28). These two identified emission peaks in 2015–2016 and 2019–2020 are consistently reflected in both bottom-up inventories, and satellite observations of HCHO and isoprene concentrations (Fig. S29). Based on these dynamics, we classify the study period into four phases: Phase I: 2013–2014 (average: 447 TgC yr⁻¹); Phase II: 2015–2016 (456 TgC yr⁻¹); Phase III: 2017–2018 (445 TgC yr⁻¹); and Phase IV:

2019–2020 (478 TgC yr⁻¹), to enable clearer analyses and to isolate the distinct emission anomalies associated with major climate events.

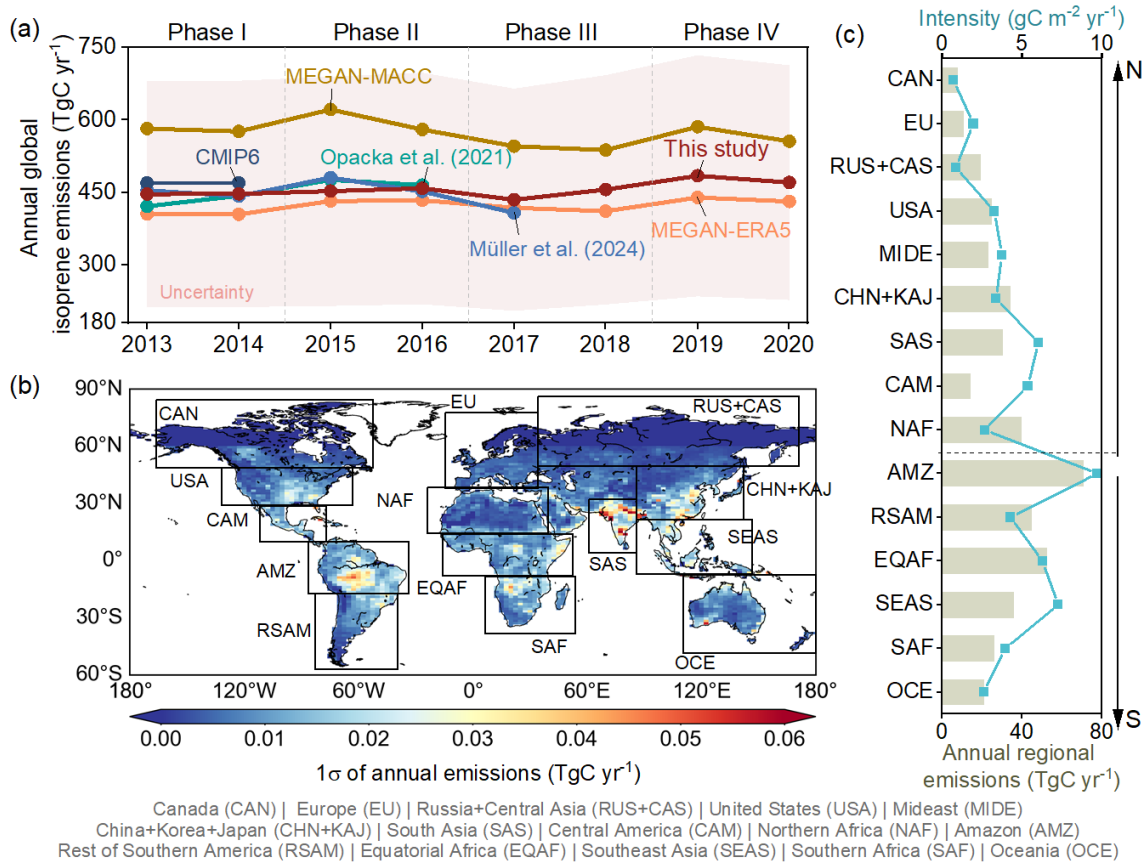


Figure 4. Interannual isoprene emission variations from 2013 to 2020. (a) compares the annual global isoprene emissions among the posterior (red shadow indicate the uncertainty), inventories including MEGAN-MACC, the MEGAN-ERA5 (also known as CAMS-GLOB-BIOv3.1) inventory, ensembles from Opacka et al. (2021), ensembles from CMIP6 (Do et al., 2025), and inversions based on corrected OMI HCHO observations (Müller et al., 2024). (b) plots the global spatial distribution of 1σ of annual isoprene emissions from 2013 to 2020, with frames corresponding to regions discussed in text. (c) depicts the regional annual emissions as well as the emission intensities (defined as the annual isoprene emissions per square meter per year). The regional classification is detailed in Fig. S6 of the SI and full names are listed below the figure.

3.5 Regional contribution to global interannual variations

Tropical regions emerge as the dominant drivers of interannual variability in global isoprene emissions, with the AMZ and RSAM identified as the largest contributors. From Phase I to IV, global emissions exhibit stepwise changes of +2.0%, -2.2%, and +7.2% relative to the preceding phase (Fig. 5a). Regional decomposition shows that the AMZ and RSAM together account for most of these changes: +7 TgC (80.9% of the global increase) during Phase I–II, -9 TgC (89.3% of the global decrease) during Phase II–III, and +9 TgC (27.7% of the global increase) during Phase III–IV. Their dominant influence reflects strong temperature sensitivity (9.0–25.5 TgC K⁻¹) (Figs. 5b–5d) and large interannual climate variability, particularly during the 2015–2016 El Niño, the following cooling, and the 2019–2020 heat events (Figs. S27–S28). The spatial patterns confirm this feature, with the largest emission fluctuations centered over the core Amazon

(Fig. 6a). Not all tropical regions exert such impacts on global interannual variations. EQAF and SEAS display limited changes, contributing +1 TgC (7.5%) to the global increase during Phase I–II but offsetting 5.3% of the global decrease in Phase II–III with a net positive change of +1 TgC (Fig. 5a). This muted response reflects regional heterogeneity in climate anomalies and ecosystem characteristics. EQAF, dominated by grasslands (55.4%) and experiencing minor temperature anomalies during El Niño (Liu et al., 2017), shows little emission change (Fig. 6b). In SEAS, widespread peatland fires in 2015 (Field et al., 2016), likely triggered by extremely low precipitation (6.5 mm, 1.5σ below the mean; Fig. S32), may have suppressed biogenic isoprene emissions in Phase II through vegetation loss and ecosystem disturbance (Ciccioli et al., 2014). Both regions, however, exhibit emission increases in Phase IV, coinciding with widespread warming ($\sim 1.0\sigma$ above their respective means) (Figs. 6b and S28).

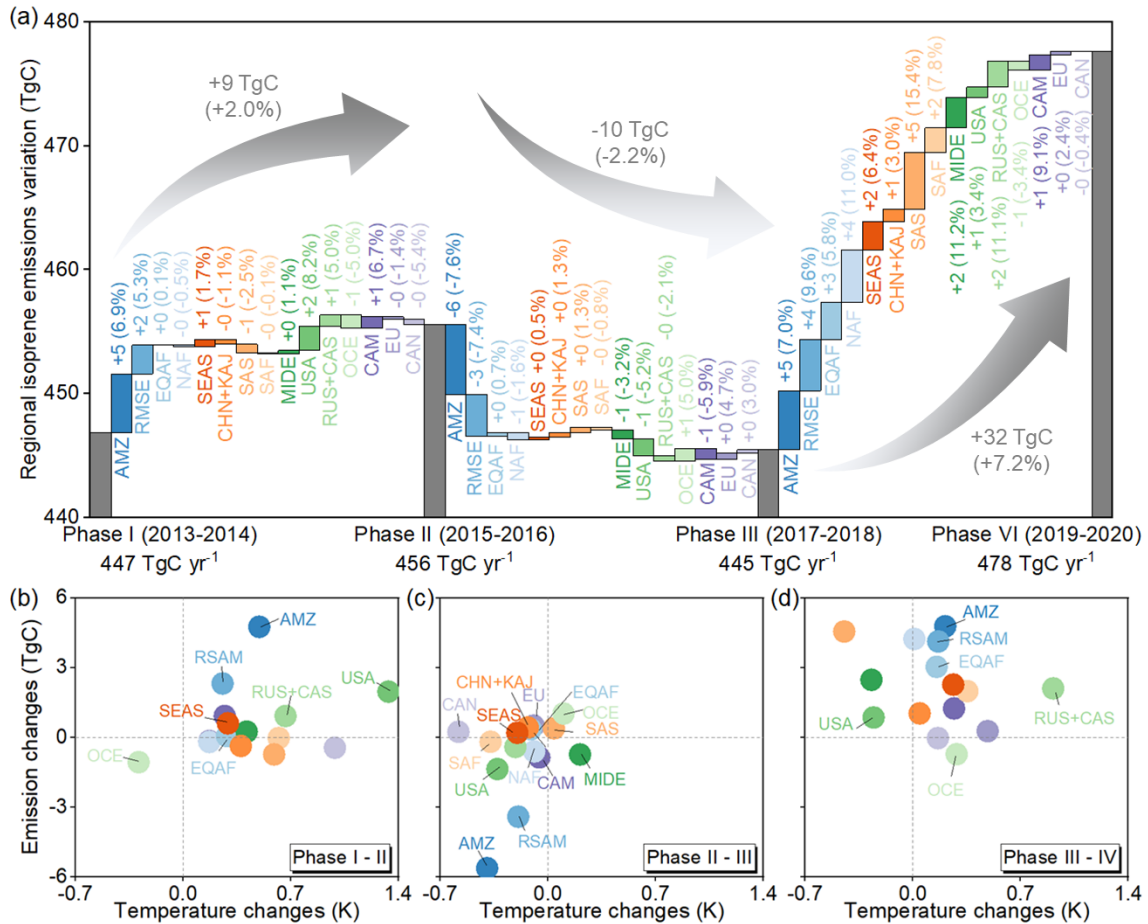


Figure 5. Regional isoprene emission variations and meteorological changes over four phases. (a) presents the regional isoprene emission variation over four phases. (b)-(d) are the scatter plots between changes in regional isoprene emissions and annual temperature from Phase I to II, II to III, and III to IV, respectively. (a)-(d) share the same legend, with colors referring to different regions. Scatter plot of changes in regional isoprene emissions and Standardised Precipitation-Evapotranspiration Index (SPEI), LAI, and radiation across phases are presented in Fig. S30.

Occasionally, non-tropical regions also contribute to the global interannual variability through extreme anomalies. In the USA, emissions increased by 2 TgC (+8.2%) from Phase I to II, making it the third largest contributor to the global increase during this period. In 2016, USA temperatures reached 285.8 K, 1.3σ above

its long-term mean (Fig. S28) and the highest warming observed among all regions during the 2015–2016 El Niño. This temperature rise, coupled with enhanced LAI (+0.05) and stable hydrological conditions (Fig. S30), favored increased photosynthetic activity and isoprene biosynthesis, elevating USA’s contribution to Phase II variability. The strong temperature sensitivity of USA isoprene emissions is consistent with previous study (Abbot et al., 2003). Conversely, OCE stands out as an exception to the global trend with emission changes of -1 TgC (-5.0%), $+1$ TgC ($+5.0\%$), and -1 TgC (-3.4%). This pattern is linked to its temperature changes (Figs. 5b-5d, S28, and S33), cooling during Phase II (-0.3 K and 1.1σ below its mean in 2016) and subsequent temperature rebound ($+0.1$ K) in Phase III (Figs. 5c and 6c). The Phase IV decline is likely linked to concurrent reductions in vegetation cover and intensified drought, particularly over northern Australia, where LAI and SPEI decreased by around 0.1-0.2 and 0.5-1, respectively (Figs. S34–S35).

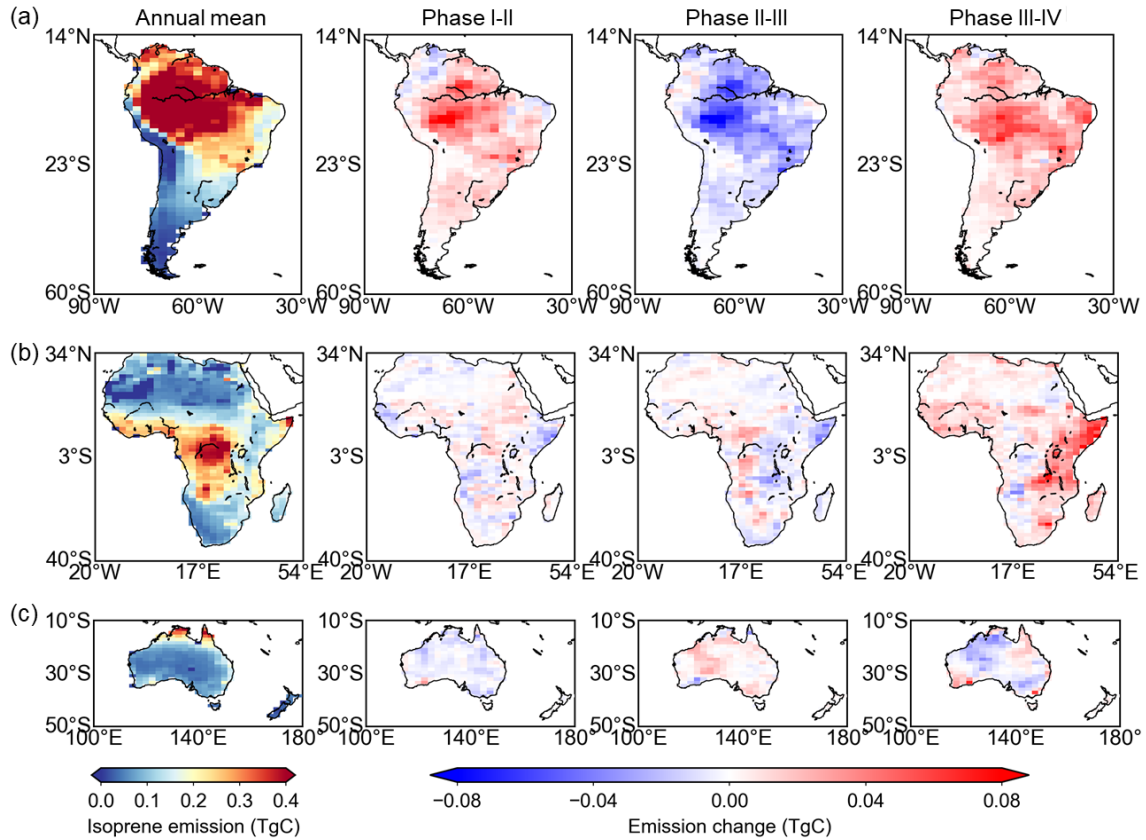


Figure 6. Regional annual mean emissions and their changes across phases for (a) Southern America including AMZ and RSAM, (b) Africa including NAF, EQAF, and SAF, and (c) OCE. The first column shows the annual mean isoprene emissions for each region, and the second to fourth columns correspond to the changes in regional isoprene emission across phases. Corresponding temperature, LAI, and SPEI distributions are shown in Figs. S33, S34, and S35.

3.6 Drivers of regional isoprene emissions on a monthly scale

To elucidate the underlying mechanisms and quantify regional sensitivities, we analyze R between monthly isoprene emissions and key environmental variables, including temperature, solar radiation, LAI (Pu et al., 2024), and drought index of Standardised Precipitation-Evapotranspiration Index (SPEI) (ECMWF, 2025), using both raw monthly values and monthly anomalies (calculated by removing the 2013-2020 mean

seasonal cycle for each month) (Figs. 7a–7b). To further assess whether temperature acts independently or interacts with other factors, partial correlation analyses are performed (Figs. 7c–7d). Although biogenic emission processes are inherently non-linear, these correlation analyses provide a useful first-order approximation of regional sensitivities within the dynamic range observed in this study period.

Across most regions, isoprene emissions show strong positive correlations with temperature ($R > 0.5$, $p < 0.05$; Fig. 7a), suggesting temperature as the dominant first-order driver. Similar patterns are also observed in the MEGAN-ERA5 inventory (Fig. S36). However, a notable difference appears in EQAF, where our posterior results show no significant correlation with temperature, whereas MEGAN-ERA5 exhibits a strong positive correlation. This finding is consistent with previous HCHO-based isoprene inversion studies, which reported a reduced temperature dependence of isoprene emissions in the EQAF region (emission factor decreased from 4.3 to 2.7 for evergreen broadleaf trees) (Marais et al., 2014). Partial correlation analysis (Fig. 7c) reveals that in many regions, including EU, MIDE, SAS, CAM, NAF, SEAS, and SAF, temperature remains the primary independent driver of emissions (partial $R > 0.5$, $p < 0.05$). In contrast, in regions such as CAN, USA, RUS+CAS, CHN+KAJ, AMZ, RSAM, and OCE, the temperature–isoprene relationships weaken or become insignificant after controlling for other factors, suggesting that co-regulators such as radiation and vegetation dynamics modulate this relationship. For example, in AMZ, the temperature–isoprene correlation becomes insignificant when controlling for radiation ($T|Rad$, $p > 0.05$), suggesting radiation as a key co-regulator, consistent with the amplified temperature response observed in Phase IV. EQAF presents a unique case: although no significant direct correlation with temperature is found, a positive partial correlation emerges when controlling for LAI ($T|LAI$ $R = 0.42$), implying that vegetation dynamics may obscure the underlying temperature sensitivity.

When monthly anomalies are used to isolate interannual variability (Figs. 7b and 7d), correlations between temperature and isoprene emissions generally weaken, indicating that the strong monthly correlations largely reflect seasonal co-variation. In most regions, temperature anomalies generally remain the dominant driver ($R > 0$, $p < 0.05$), albeit with weaker correlations than for the raw monthly values. Notably, AMZ ($R = 0.79$) and OCE ($R = 0.70$) retain significant temperature–isoprene coupling, reflecting robust interannual temperature sensitivity. In regions where temperature anomalies fail to explain interannual variability (e.g., SAS, CAN, RUS+CAS), other drivers emerge. For instance, in SAS, LAI anomalies show the strongest association with isoprene anomalies ($R = 0.65$), underscoring the critical role of vegetation dynamics in controlling its interannual emissions. Interestingly, in EQAF, where no significant correlation is found using raw monthly data, temperature anomalies correlate significantly with isoprene anomalies, revealing an interannual sensitivity previously masked by seasonal effects. Anomaly-based partial correlations further clarify the independent role of temperature (Fig. 7d). Where direct correlations between temperature anomalies and isoprene anomalies are significant, temperature generally remains an independent driver (partial $R > 0$, $p < 0.05$), particularly in AMZ and OCE. In contrast, in regions such as CAN, RUS+CAS, and SAS, where direct temperature–isoprene correlations are insignificant ($p > 0.05$), interannual variability is dominated by other factors. For example, in SAS, LAI anomalies exhibit the strongest ($R = 0.65$ in Fig. 7b) and most

independent association with isoprene anomalies, even after controlling for other variables ($R=0.49-0.80$), underscoring the dominant role of vegetation dynamics in modulating interannual emissions in this region.

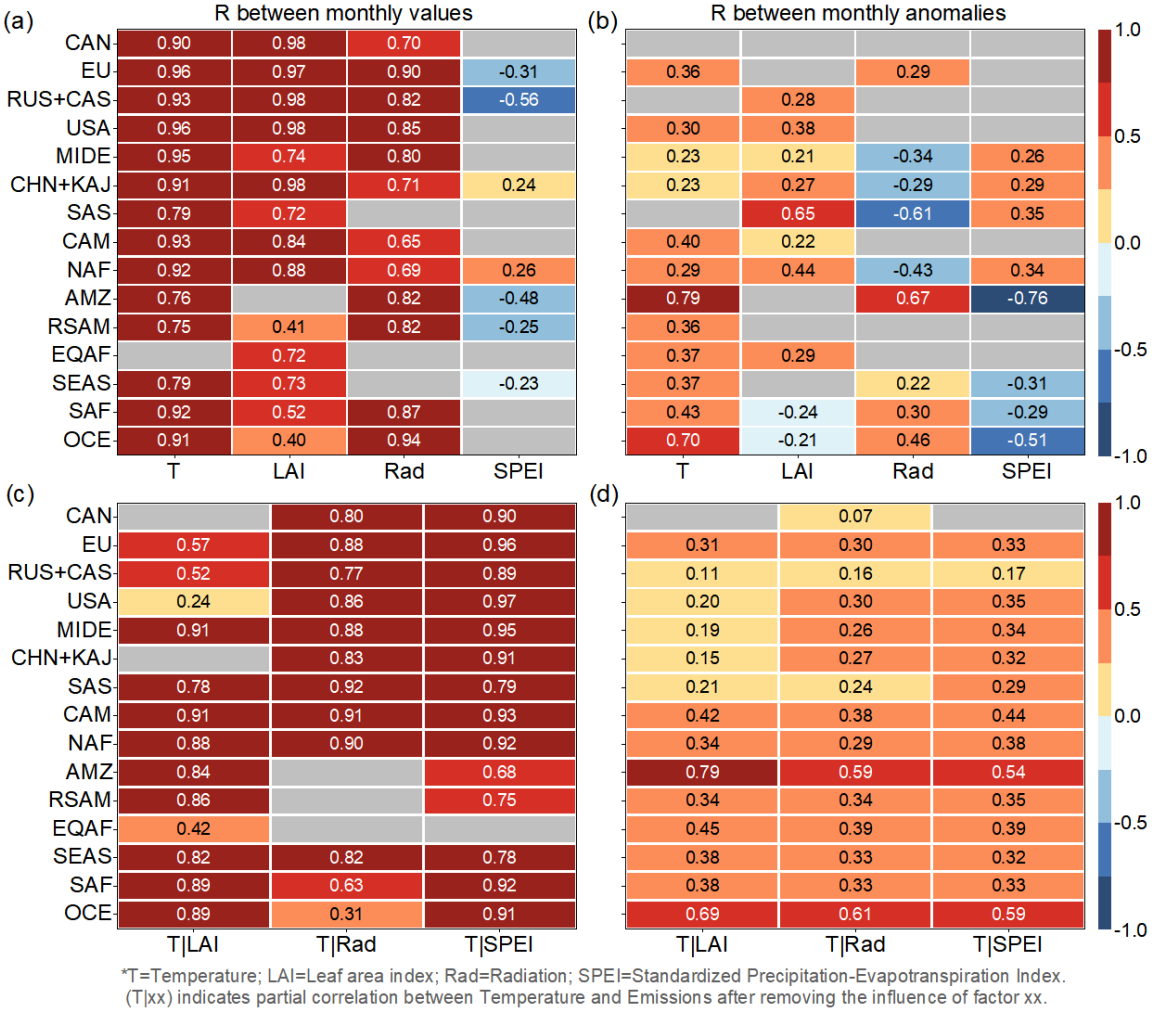


Figure 7. Pearson correlation (R) matrix between regional isoprene emissions and environmental factors on a monthly scale. (a) shows the R matrix between monthly regional isoprene emissions and environmental factors. (c) plots the partial correlation coefficient between temperature and isoprene emissions after removing certain factor's impact. (b) and (d) are plotted for monthly anomalies obtained by removing the mean seasonal cycle as (a) and (c). In all panels, T and Rad represent temperature and radiation, respectively. Regions are ordered from south to north (bottom to top). Gray boxes indicate non-significant correlations ($p>0.05$).

Overall, temperature exerts the primary control on regional isoprene variability, but its apparent influence is regionally modulated by co-varying environmental factors, particularly radiation and vegetation activity. The anomaly-based correlations provide clearer evidence that while the apparent temperature dependence partly reflects seasonal co-variation, interannual variability in tropical and subtropical regions is primarily governed by coupled changes in temperature and ecosystem conditions.

4. Limitations

While our results demonstrate clear improvements over prior estimates in terms of both spatial distribution and correlation with observations (Figs. 1 and S17-S19), several limitations remain, highlighting areas for future refinement. A primary limitation arises from the incomplete spatial coverage of CrIS observations, particularly at high latitudes (north of 60°N; Fig. S1), where emissions in this study remain unchanged from prior. This omission has limited impact on global totals (~1.0% in prior), as boreal and tundra emissions are minor compared to tropical regions (Guenther et al., 2012). However, warming-driven increases in Arctic isoprene emissions (Seco et al., 2022; Wang et al., 2024d) suggest these regions may become more important in future global budgets and merit closer attention in upcoming inversions. Another limitation stems from comparing CrIS-retrieved isoprene columns with model outputs, as both are subject to uncertainties. The ANN-based retrieval lacks scene-specific vertical sensitivity information, introducing additional uncertainty in aligning the vertical profiles between observations and the model. Similarly, uncertainties in the LMDZ-INCA model's treatment of isoprene chemistry and transport may propagate into simulated columns. Moreover, relying on a single model framework introduces structural uncertainty that cannot be fully quantified here. Model-specific formulations of boundary layer mixing, photochemistry, and deposition can affect the simulated column–emission relationships. These issues could be mitigated through retrievals that include vertical sensitivity information, continued model development, and cross-model ensemble evaluations to better represent atmospheric isoprene processes.

Beyond satellite-related issues, several methodological constraints inherent to the inversion framework must be acknowledged. The FDM approach assumes a localized linear relationship between surface emissions and atmospheric column concentrations, which simplifies the complex, non-linear chemistry of isoprene. This assumption is partly justified because CrIS observations are acquired near 13:30 local time, when OH concentrations peak and isoprene lifetimes are shortest (Hard et al., 1986; Karl et al., 2004). Moreover, this linearization is supported by sensitivity tests with varying perturbation magnitudes, increased NO_x emission input, and improved posterior fits to CrIS observations. Nevertheless, the linearity between isoprene columns and emissions may break down across regions, especially in high-isoprene, low-NO_x environment like the Amazon, where OH levels are limited (Zhao et al., 2025; Yoon, 2025). Future work could adopt joint NO_x–isoprene inversions or iterative schemes (Wells et al., 2020), to better capture the strong chemical coupling between NO_x, OH, and isoprene.

5. Data and code availability

All the data and model code are openly available. The isoprene emission data in this study are deposited in Zenodo (<https://doi.org/10.5281/zenodo.16214776>) (Hui et al., 2025). Other data include: the OMPS HCHO products are available in the NASA GES DISC for OMPS/Suomi-NPP (<https://doi.org/10.5067/IIM1GHT07QA8>); the TROPOMI HCHO products are available at <https://sentiwiki.copernicus.eu/web/s5p-products>; the 2013–2020 climatological means of the CrIS

isoprene columns are available at <https://doi.org/10.13020/5n0j-wx73> (Wells et al., 2022). All the meteorological factors (temperature, precipitation, and radiation) are acquired from ERA5 dataset at <https://cds.climate.copernicus.eu/datasets/reanalysis-era5-land-monthly-means?tab=overview>. Land cover data from 2013 to 2020 are ESA Land Cover Climate Change Initiative (Land_Cover_cci): Global Plant Functional Types (PFT) Dataset, v2.0.8, acquired from <https://catalogue.ceda.ac.uk/uuid/26a0f46c95ee4c29b5c650b129aab788/>. Pandonia Global Network (PGN) surface observed HCHO area acquired from <https://www.pandonia-global-network.org/>. The drought indices, i.e., the Standardised Precipitation-Evapotranspiration Index (SPEI), are obtained from ECMWF (<https://xds-preprod.ecmwf.int/datasets/derived-drought-historical-monthly?tab=overview>). Leaf area index (LAI) data are acquired from Pu et al. (2024). The codes and scripts developed for inversions, plotting, and other analysis are accessible upon reasonable request from the corresponding author. The version of the LMDZ-INCA model used in this study is available from: <https://forge.ipsl.jussieu.fr/igcmg/svn/modipsl/trunk>.

6. Implication

This study provides, to our knowledge, the first global, multi-year (2013–2020) estimates of isoprene emissions derived directly from satellite-retrieved isoprene concentrations, offering valuable insights into the temporal and spatial drivers of emission variability. Our analysis reveals the dominant influence of climate anomalies in shaping both global and regional variability. On interannual timescales, two major emission peaks in 2015–2016 and 2019–2020 coincide with El Niño and widespread extreme heat events, driven primarily by temperature-induced enhancements in tropical regions, especially the Amazon. The elevated biogenic isoprene emissions during the El Niño period are consistent with previous studies (Lathière et al., 2006; Naik et al., 2004). Seasonally, global emissions peak during July–September (JAS) and reach a minimum in December–February (DJF), reflecting the pronounced seasonality of temperature and vegetation activity in the Northern Hemisphere. This seasonal pattern contrasts with the JAS minimum and DJF peak simulated by the two MEGAN inventories. Sensitivity inversions using MEGAN-MACC and MEGAN-ERA5 as priors yield consistent posterior seasonality, suggesting that bottom-up inventories likely overestimate emissions in the Southern Hemisphere, especially over Oceania. Regarding temperature sensitivity, MEGAN-based emissions generally display a more uniform response to temperature, whereas our inversion indicates regionally differentiated sensitivities. For instance, in EQAF, temperature is not the apparent dominant driver, implying that other factors, such as vegetation dynamics or solar radiation, exert a stronger influence than represented in current models.

Given the sub-decadal scope of this study, the analysis has focused on short-term climate variability, especially temperature, as the principal driver, while long-term influences such as land cover change and rising atmospheric CO₂ concentrations are not explicitly addressed. Extending this framework to multi-decadal periods will be essential to disentangle the interplay between short- and long-term drivers and to assess their combined impacts on atmospheric chemistry and climate feedbacks. The occurrence of two major

climate anomalies, El Niño and widespread extreme heat events, supports the focus on extreme weather, which exerts disproportionate impacts on isoprene emissions. Looking ahead, however, the convergence of multiple environmental stressors, including global warming (Armstrong McKay et al., 2022), deforestation in tropical regions (Leite-Filho et al., 2021), rising atmospheric CO₂ (with its dual fertilization and inhibition effects) (Cheng et al., 2022; Sahu et al., 2023), and the increasing frequency and intensity of climate extremes (wildfires, floods, and droughts) (Newman and Noy, 2023; Gebrechorkos et al., 2025; Zheng et al., 2023), raise critical questions about the long-term trajectory of global isoprene emissions. A key uncertainty is whether these interacting pressures will collectively amplify or suppress future emissions. Given isoprene's central role in regulating atmospheric oxidative capacity, such dynamics profoundly influence broader climate feedbacks. For instance, a sustained decline in isoprene emissions may elevate OH radical concentrations, thereby accelerating the atmospheric removal of CH₄ and other species (Zhao et al., 2025). However, the magnitude and direction of such feedbacks remain poorly constrained, highlighting the need for continued advancements in satellite observations and modeling tools to better characterize isoprene emissions and their interactions within the coupled biosphere–atmosphere system under future climate scenarios.

Acknowledgements

This work was supported by the National Key R&D Program of China (Grant Nos. 2023YFC3709202), was granted access to the HPC resources of TGCC under the allocation A0170102201 made by GENCI, and was funded by ESA WORlD Emission (WOREM) project (<https://www.world-emission.com>). We wish to thank J. Bruna (LSCE) and his team for computer support and the use of the OBELIX computing facility at LSCE, and thank Juliette Lathiere (LSCE) and her team for providing ORCHIDEE biogenic volatile organic compounds emissions. DBM and KCW acknowledge support from NASA GMAO (grant #80NSSC23K0520).

Author contributions

HL designed this study, conducted the emission inversions, analyzed the data, and wrote the draft. PC, DH, BZ, and GB supervised the study, helped data analysis, reviewed and edited the paper. PK performed the LMDZ-INCA simulations, helped data analysis, and edited the paper. DB and KW offered the CrIS isoprene data, reviewed and edited the paper. FC and JL reviewed and edited the paper. All the co-authors contributed to the revision of this paper.

Competing interests

At least one of the (co-)authors is a member of the editorial board of *Earth System Science Data*. The authors have no other competing interests to declare.

649 **Reference**

- 650 Abad, G. G.: OMPS-NPP L2 NM Formaldehyde (HCHO) Total Column swath orbital V1, Greenbelt,
651 MD, USA, Goddard Earth Sciences Data and Information Services Center (GES DISC),
652 10.5067/IIM1GHT07QA8, 2022.
- 653 Abbot, D. S., Palmer, P. I., Martin, R. V., Chance, K. V., Jacob, D. J., and Guenther, A.: Seasonal and
654 interannual variability of North American isoprene emissions as determined by formaldehyde
655 column measurements from space, *Geophysical Research Letters*, 30,
656 <https://doi.org/10.1029/2003GL017336>, 2003.
- 657 Armstrong McKay, D. I., Staal, A., Abrams, J. F., Winkelmann, R., Sakschewski, B., Loriani, S., Fetzer,
658 I., Cornell, S. E., Rockström, J., and Lenton, T. M.: Exceeding 1.5°C global warming could trigger
659 multiple climate tipping points, *Science*, 377, eabn7950, doi:10.1126/science.abn7950, 2022.
- 660 Barkley, M. P., Smedt, I. D., Van Roozendaal, M., Kurosu, T. P., Chance, K., Arneth, A., Hagberg, D.,
661 Guenther, A., Paulot, F., Marais, E., et al.: Top-down isoprene emissions over tropical South
662 America inferred from SCIAMACHY and OMI formaldehyde columns, *Journal of Geophysical*
663 *Research: Atmospheres*, 118, 6849-6868, <https://doi.org/10.1002/jgrd.50552>, 2013.
- 664 Bates, K. H. and Jacob, D. J.: A new model mechanism for atmospheric oxidation of isoprene:
665 global effects on oxidants, nitrogen oxides, organic products, and secondary organic aerosol,
666 *Atmos. Chem. Phys.*, 19, 9613-9640, 10.5194/acp-19-9613-2019, 2019.
- 667 Bauwens, M., Stavrakou, T., Müller, J. F., De Smedt, I., Van Roozendaal, M., van der Werf, G. R.,
668 Wiedinmyer, C., Kaiser, J. W., Sindelarova, K., and Guenther, A.: Nine years of global hydrocarbon
669 emissions based on source inversion of OMI formaldehyde observations, *Atmos. Chem. Phys.*, 16,
670 10133-10158, 10.5194/acp-16-10133-2016, 2016.
- 671 Cao, Y., Yue, X., Lei, Y., Zhou, H., Liao, H., Song, Y., Bai, J., Yang, Y., Chen, L., Zhu, J., et al.: Identifying
672 the Drivers of Modeling Uncertainties in Isoprene Emissions: Schemes Versus Meteorological
673 Forcings, *Journal of Geophysical Research: Atmospheres*, 126, e2020JD034242,
674 <https://doi.org/10.1029/2020JD034242>, 2021.
- 675 Cheng, W., Dan, L., Deng, X., Feng, J., Wang, Y., Peng, J., Tian, J., Qi, W., Liu, Z., Zheng, X., et al.:
676 Global monthly gridded atmospheric carbon dioxide concentrations under the historical and
677 future scenarios, *Scientific Data*, 9, 83, 10.1038/s41597-022-01196-7, 2022.
- 678 Choi, J., Henze, D. K., Wells, K. C., and Millet, D. B.: Joint Inversion of Satellite-Based Isoprene and
679 Formaldehyde Observations to Constrain Emissions of Nonmethane Volatile Organic Compounds,
680 *Journal of Geophysical Research: Atmospheres*, 130, e2024JD042070,
681 <https://doi.org/10.1029/2024JD042070>, 2025.
- 682 Ciccioli, P., Centritto, M., and Loreto, F.: Biogenic volatile organic compound emissions from
683 vegetation fires, *Plant, Cell & Environment*, 37, 1810-1825, <https://doi.org/10.1111/pce.12336>,
684 2014.
- 685 Cooper, M., Martin, R. V., Padmanabhan, A., and Henze, D. K.: Comparing mass balance and
686 adjoint methods for inverse modeling of nitrogen dioxide columns for global nitrogen oxide
687 emissions, *Journal of Geophysical Research: Atmospheres*, 122, 4718-4734,
688 <https://doi.org/10.1002/2016JD025985>, 2017.
- 689 Curtius, J., Heinritzi, M., Beck, L. J., Pöhlker, M. L., Tripathi, N., Krumm, B. E., Holzbeck, P.,
690 Nussbaumer, C. M., Hernández Pardo, L., Klimach, T., et al.: Isoprene nitrates drive new particle
691 formation in Amazon's upper troposphere, *Nature*, 636, 124-130, 10.1038/s41586-024-08192-4,
692 2024.
- 693 Do, N. T. N., Sudo, K., Ito, A., Emmons, L. K., Naik, V., Tsigaridis, K., Seland, Ø., Folberth, G. A., and
694 Kelley, D. I.: Historical trends and controlling factors of isoprene emissions in CMIP6 Earth system
695 models, *Geosci. Model Dev.*, 18, 2079-2109, 10.5194/gmd-18-2079-2025, 2025.

ECMWF: Monthly drought indices from 1940 to present derived from ERA5 reanalysis. ECMWF Cross Data Store (ECDS). 10.24381/9bea5e16 (Accessed on 06-06-2025), 2025.

Emmerson, K. M., Cope, M. E., Galbally, I. E., Lee, S., and Nelson, P. F.: Isoprene and monoterpene emissions in south-east Australia: comparison of a multi-layer canopy model with MEGAN and with atmospheric observations, *Atmos. Chem. Phys.*, 18, 7539-7556, 10.5194/acp-18-7539-2018, 2018.

Emmerson, K. M., Galbally, I. E., Guenther, A. B., Paton-Walsh, C., Guerette, E. A., Cope, M. E., Keywood, M. D., Lawson, S. J., Molloy, S. B., Dunne, E., et al.: Current estimates of biogenic emissions from eucalypts uncertain for southeast Australia, *Atmos. Chem. Phys.*, 16, 6997-7011, 10.5194/acp-16-6997-2016, 2016.

ESA: S5P_L2__HCHO__HiR. Version 2. Sentinel-5P TROPOMI Tropospheric Formaldehyde HCHO 1-Orbit L2 5.5km x 3.5km. Greenbelt, MD, USA. Archived by National Aeronautics and Space Administration, U.S. Government, Goddard Earth Sciences Data and Information Services Center (GES DISC). 10.5270/S5P-vg1i7t0, 2020.

Field, R. D., van der Werf, G. R., Fanin, T., Fetzer, E. J., Fuller, R., Jethva, H., Levy, R., Livesey, N. J., Luo, M., Torres, O., et al.: Indonesian fire activity and smoke pollution in 2015 show persistent nonlinear sensitivity to El Niño-induced drought, *Proceedings of the National Academy of Sciences*, 113, 9204-9209, doi:10.1073/pnas.1524888113, 2016.

Folberth, G. A., Hauglustaine, D. A., Lathière, J., and Brocheton, F.: Interactive chemistry in the Laboratoire de Météorologie Dynamique general circulation model: model description and impact analysis of biogenic hydrocarbons on tropospheric chemistry, *Atmos. Chem. Phys.*, 6, 2273-2319, 10.5194/acp-6-2273-2006, 2006.

Fu, D., Millet, D. B., Wells, K. C., Payne, V. H., Yu, S., Guenther, A., and Eldering, A.: Direct retrieval of isoprene from satellite-based infrared measurements, *Nature Communications*, 10, 3811, 10.1038/s41467-019-11835-0, 2019.

Gebrechorkos, S. H., Sheffield, J., Vicente-Serrano, S. M., Funk, C., Miralles, D. G., Peng, J., Dyer, E., Talib, J., Beck, H. E., Singer, M. B., et al.: Warming accelerates global drought severity, *Nature*, 10.1038/s41586-025-09047-2, 2025.

Geddes, J. A., Pusede, S. E., and Wong, A. Y. H.: Changes in the Relative Importance of Biogenic Isoprene and Soil NO_x Emissions on Ozone Concentrations in Nonattainment Areas of the United States, *Journal of Geophysical Research: Atmospheres*, 127, e2021JD036361, <https://doi.org/10.1029/2021JD036361>, 2022.

Gomes Alves, E., Aquino Santana, R., Quaresma Dias-Júnior, C., Botía, S., Taylor, T., Yáñez-Serrano, A. M., Kesselmeier, J., Bourtsoukidis, E., Williams, J., Lembo Silveira de Assis, P. I., et al.: Intra- and interannual changes in isoprene emission from central Amazonia, *Atmos. Chem. Phys.*, 23, 8149-8168, 10.5194/acp-23-8149-2023, 2023.

Guenther, A. B., Jiang, X., Heald, C. L., Sakulyanontvittaya, T., Duhl, T., Emmons, L. K., and Wang, X.: The Model of Emissions of Gases and Aerosols from Nature version 2.1 (MEGAN2.1): an extended and updated framework for modeling biogenic emissions, *Geosci. Model Dev.*, 5, 1471-1492, 10.5194/gmd-5-1471-2012, 2012.

Hard, T. M., Chan, C. Y., Mehrabzadeh, A. A., Pan, W. H., and O'Brien, R. J.: Diurnal cycle of tropospheric OH, *Nature*, 322, 617-620, 10.1038/322617a0, 1986.

Hauglustaine, D. A., Hourdin, F., Jourdain, L., Filiberti, M. A., Walters, S., Lamarque, J. F., and Holland, E. A.: Interactive chemistry in the Laboratoire de Météorologie Dynamique general circulation model: Description and background tropospheric chemistry evaluation, *Journal of Geophysical Research: Atmospheres*, 109, <https://doi.org/10.1029/2003JD003957>, 2004.

742 Henrot, A. J., Stanelle, T., Schröder, S., Siegenthaler, C., Taraborrelli, D., and Schultz, M. G.:
 743 Implementation of the MEGAN (v2.1) biogenic emission model in the ECHAM6-HAMMOZ
 744 chemistry climate model, *Geosci. Model Dev.*, 10, 903-926, 10.5194/gmd-10-903-2017, 2017.
 745 Hewson, W., Barkley, M. P., Gonzalez Abad, G., Bösch, H., Kurosu, T., Spurr, R., and Tilstra, L. G.:
 746 Development and characterisation of a state-of-the-art GOME-2 formaldehyde air-mass factor
 747 algorithm, *Atmos. Meas. Tech.*, 8, 4055-4074, 10.5194/amt-8-4055-2015, 2015.
 748 Hoesly, R. M., Smith, S. J., Feng, L., Klimont, Z., Janssens-Maenhout, G., Pitkanen, T., Seibert, J. J.,
 749 Vu, L., Andres, R. J., Bolt, R. M., et al.: Historical (1750–2014) anthropogenic emissions of reactive
 750 gases and aerosols from the Community Emissions Data System (CEDS), *Geosci. Model Dev.*, 11,
 751 369-408, 10.5194/gmd-11-369-2018, 2018.
 752 Hu, S. and Fedorov, A. V.: The extreme El Niño of 2015–2016 and the end of global warming hiatus,
 753 *Geophysical Research Letters*, 44, 3816-3824, <https://doi.org/10.1002/2017GL072908>, 2017.
 754 Hui, L., Philippe, C., Pramod, K., Didier A., H., Frédéric, C., Grégoire, B., Dylan B., M., Kelley C., W.,
 755 Jinghui, L., and Bo, Z.: Global biogenic isoprene emissions 2013-2020 inferred from satellite
 756 isoprene observations, *Zenodo.*, <https://doi.org/10.5281/zenodo.16214776>, 2025.
 757 Kaiser, J., Jacob, D. J., Zhu, L., Travis, K. R., Fisher, J. A., González Abad, G., Zhang, L., Zhang, X.,
 758 Fried, A., Crounse, J. D., et al.: High-resolution inversion of OMI formaldehyde columns to quantify
 759 isoprene emission on ecosystem-relevant scales: application to the southeast US, *Atmos. Chem.*
 760 *Phys.*, 18, 5483-5497, 10.5194/acp-18-5483-2018, 2018.
 761 Karl, M., Brauers, T., Dorn, H. P., Holland, F., Komenda, M., Poppe, D., Rohrer, F., Rupp, L., Schaub,
 762 A., and Wahner, A.: Kinetic Study of the OH-isoprene and O₃-isoprene reaction in the atmosphere
 763 simulation chamber, SAPHIR, *Geophysical Research Letters*, 31,
 764 <https://doi.org/10.1029/2003GL019189>, 2004.
 765 Kumar, P., Broquet, G., Hauglustaine, D., Beaudor, M., Clarisse, L., Van Damme, M., Coheur, P.,
 766 Cozic, A., Zheng, B., Revilla Romero, B., et al.: Global atmospheric inversion of the NH₃ emissions
 767 over 2019-2022 using the LMDZ-INCA chemistry-transport model and the IASI NH₃ observations,
 768 *EGUsphere*, 2025, 1-32, 10.5194/egusphere-2025-162, 2025.
 769 Lathière, J., Hauglustaine, D. A., Friend, A. D., De Noblet-Ducoudré, N., Viovy, N., and Folberth, G.
 770 A.: Impact of climate variability and land use changes on global biogenic volatile organic
 771 compound emissions, *Atmos. Chem. Phys.*, 6, 2129-2146, 10.5194/acp-6-2129-2006, 2006.
 772 Leite-Filho, A. T., Soares-Filho, B. S., Davis, J. L., Abrahão, G. M., and Börner, J.: Deforestation
 773 reduces rainfall and agricultural revenues in the Brazilian Amazon, *Nature Communications*, 12,
 774 2591, 10.1038/s41467-021-22840-7, 2021.
 775 Liu, J., Bowman, K. W., Schimel, D. S., Parazoo, N. C., Jiang, Z., Lee, M., Bloom, A. A., Wunch, D.,
 776 Frankenberg, C., Sun, Y., et al.: Contrasting carbon cycle responses of the tropical continents to
 777 the 2015–2016 El Niño, *Science*, 358, eaam5690, doi:10.1126/science.aam5690, 2017.
 778 Ma, H., Crowther, T. W., Mo, L., Maynard, D. S., Renner, S. S., van den Hoogen, J., Zou, Y., Liang,
 779 J., de-Miguel, S., Nabuurs, G.-J., et al.: The global biogeography of tree leaf form and habit, *Nature*
 780 *Plants*, 9, 1795-1809, 10.1038/s41477-023-01543-5, 2023.
 781 Marais, E. A., Jacob, D. J., Guenther, A., Chance, K., Kurosu, T. P., Murphy, J. G., Reeves, C. E., and
 782 Pye, H. O. T.: Improved model of isoprene emissions in Africa using Ozone Monitoring Instrument
 783 (OMI) satellite observations of formaldehyde: implications for oxidants and particulate matter,
 784 *Atmos. Chem. Phys.*, 14, 7693-7703, 10.5194/acp-14-7693-2014, 2014.
 785 Marais, E. A., Jacob, D. J., Kurosu, T. P., Chance, K., Murphy, J. G., Reeves, C., Mills, G., Casadio, S.,
 786 Millet, D. B., Barkley, M. P., et al.: Isoprene emissions in Africa inferred from OMI observations of
 787 formaldehyde columns, *Atmos. Chem. Phys.*, 12, 6219-6235, 10.5194/acp-12-6219-2012, 2012.
 788 McDuffie, E. E., Smith, S. J., O'Rourke, P., Tibrewal, K., Venkataraman, C., Marais, E. A., Zheng, B.,
 789 Crippa, M., Brauer, M., and Martin, R. V.: A global anthropogenic emission inventory of

atmospheric pollutants from sector- and fuel-specific sources (1970–2017): an application of the Community Emissions Data System (CEDS), *Earth Syst. Sci. Data*, 12, 3413–3442, 10.5194/essd-12-3413-2020, 2020.

Mellor, G. L. and Yamada, T.: Development of a turbulence closure model for geophysical fluid problems, *Reviews of Geophysics*, 20, 851–875, <https://doi.org/10.1029/RG020i004p00851>, 1982.

Messina, P., Lathi  re, J., Sindelarova, K., Vuichard, N., Granier, C., Ghattas, J., Cozic, A., and Hauglustaine, D. A.: Global biogenic volatile organic compound emissions in the ORCHIDEE and MEGAN models and sensitivity to key parameters, *Atmos. Chem. Phys.*, 16, 14169–14202, 10.5194/acp-16-14169-2016, 2016.

Millet, D. B., Jacob, D. J., Boersma, K. F., Fu, T.-M., Kurosu, T. P., Chance, K., Heald, C. L., and Guenther, A.: Spatial distribution of isoprene emissions from North America derived from formaldehyde column measurements by the OMI satellite sensor, *Journal of Geophysical Research: Atmospheres*, 113, <https://doi.org/10.1029/2007JD008950>, 2008.

M  ller, J. F., Stavrakou, T., Oomen, G. M., Opacka, B., De Smedt, I., Guenther, A., Vigouroux, C., Langerock, B., Aquino, C. A. B., Grutter, M., et al.: Bias correction of OMI HCHO columns based on FTIR and aircraft measurements and impact on top-down emission estimates, *Atmos. Chem. Phys.*, 24, 2207–2237, 10.5194/acp-24-2207-2024, 2024.

Naik, V., Delire, C., and Wuebbles, D. J.: Sensitivity of global biogenic isoprenoid emissions to climate variability and atmospheric CO₂, *Journal of Geophysical Research: Atmospheres*, 109, <https://doi.org/10.1029/2003JD004236>, 2004.

Newman, R. and Noy, I.: The global costs of extreme weather that are attributable to climate change, *Nature Communications*, 14, 6103, 10.1038/s41467-023-41888-1, 2023.

Novelli, A., Vereecken, L., Bohn, B., Dorn, H. P., Gkatzelis, G. I., Hofzumahaus, A., Holland, F., Reimer, D., Rohrer, F., Rosanka, S., et al.: Importance of isomerization reactions for OH radical regeneration from the photo-oxidation of isoprene investigated in the atmospheric simulation chamber SAPHIR, *Atmos. Chem. Phys.*, 20, 3333–3355, 10.5194/acp-20-3333-2020, 2020.

Nowlan, C. R., Gonz  lez Abad, G., Kwon, H.-A., Ayazpour, Z., Chan Miller, C., Chance, K., Chong, H., Liu, X., O’Sullivan, E., Wang, H., et al.: Global Formaldehyde Products From the Ozone Mapping and Profiler Suite (OMPS) Nadir Mappers on Suomi NPP and NOAA-20, *Earth and Space Science*, 10, e2022EA002643, <https://doi.org/10.1029/2022EA002643>, 2023.

Nussbaumer, C. M., Crowley, J. N., Schuladen, J., Williams, J., Hafermann, S., Reiffs, A., Axinte, R., Harder, H., Ernest, C., Novelli, A., et al.: Measurement report: Photochemical production and loss rates of formaldehyde and ozone across Europe, *Atmos. Chem. Phys.*, 21, 18413–18432, 10.5194/acp-21-18413-2021, 2021.

Opacka, B., M  ller, J. F., Stavrakou, T., Bauwens, M., Sindelarova, K., Markova, J., and Guenther, A. B.: Global and regional impacts of land cover changes on isoprene emissions derived from spaceborne data and the MEGAN model, *Atmos. Chem. Phys.*, 21, 8413–8436, 10.5194/acp-21-8413-2021, 2021.

Pacifico, F., Folberth, G. A., Jones, C. D., Harrison, S. P., and Collins, W. J.: Sensitivity of biogenic isoprene emissions to past, present, and future environmental conditions and implications for atmospheric chemistry, *Journal of Geophysical Research: Atmospheres*, 117, <https://doi.org/10.1029/2012JD018276>, 2012.

Palmer, P. I., Marvin, M. R., Siddans, R., Kerridge, B. J., and Moore, D. P.: Nocturnal survival of isoprene linked to formation of upper tropospheric organic aerosol, *Science*, 375, 562–566, 10.1126/science.abg4506, 2022.

Pletzer, J., Hauglustaine, D., Cohen, Y., J  ckel, P., and Grewe, V.: The climate impact of hydrogen-powered hypersonic transport, *Atmos. Chem. Phys.*, 22, 14323–14354, 10.5194/acp-22-14323-2022, 2022.

838 Pound, R. J., Durcan, D. P., Evans, M. J., and Carpenter, L. J.: Comparing the Importance of Iodine
839 and Isoprene on Tropospheric Photochemistry, *Geophysical Research Letters*, 50,
840 e2022GL100997, <https://doi.org/10.1029/2022GL100997>, 2023.

841 Pu, J., Yan, K., Roy, S., Zhu, Z., Rautiainen, M., Knyazikhin, Y., and Myneni, R. B.: Sensor-
842 independent LAI/FPAR CDR: reconstructing a global sensor-independent climate data record of
843 MODIS and VIIRS LAI/FPAR from 2000 to 2022, *Earth Syst. Sci. Data*, 16, 15-34, 10.5194/essd-16-
844 15-2024, 2024.

845 Ren, Y., Qiu, J., Zeng, Z., Liu, X., Sitch, S., Pilegaard, K., Yang, T., Wang, S., Yuan, W., and Jain, A. K.:
846 Earlier spring greening in Northern Hemisphere terrestrial biomes enhanced net ecosystem
847 productivity in summer, *Communications Earth & Environment*, 5, 122, 10.1038/s43247-024-
848 01270-5, 2024.

849 Robinson, A., Lehmann, J., Barriopedro, D., Rahmstorf, S., and Coumou, D.: Increasing heat and
850 rainfall extremes now far outside the historical climate, *npj Climate and Atmospheric Science*, 4,
851 45, 10.1038/s41612-021-00202-w, 2021.

852 Sahu, A., Mostofa, M. G., Weraduwege, S. M., and Sharkey, T. D.: Hydroxymethylbutenyl
853 diphosphate accumulation reveals MEP pathway regulation for high CO₂-induced suppression of
854 isoprene emission, *Proceedings of the National Academy of Sciences*, 120, e2309536120,
855 doi:10.1073/pnas.2309536120, 2023.

856 Sand, M., Skeie, R. B., Sandstad, M., Krishnan, S., Myhre, G., Bryant, H., Derwent, R., Hauglustaine,
857 D., Paulot, F., Prather, M., et al.: A multi-model assessment of the Global Warming Potential of
858 hydrogen, *Communications Earth & Environment*, 4, 203, 10.1038/s43247-023-00857-8, 2023.

859 Seco, R., Holst, T., Davie-Martin, C. L., Simin, T., Guenther, A., Pirk, N., Rinne, J., and Rinnan, R.:
860 Strong isoprene emission response to temperature in tundra vegetation, *Proceedings of the*
861 *National Academy of Sciences*, 119, e2118014119, doi:10.1073/pnas.2118014119, 2022.

862 Sindelarova, K., Markova, J., Simpson, D., Huszar, P., Karlicky, J., Darras, S., and Granier, C.: High-
863 resolution biogenic global emission inventory for the time period 2000–2019 for air quality
864 modelling, *Earth Syst. Sci. Data*, 14, 251-270, 10.5194/essd-14-251-2022, 2022.

865 Sindelarova, K., Granier, C., Bouarar, I., Guenther, A., Tilmes, S., Stavrou, T., Müller, J. F., Kuhn,
866 U., Stefani, P., and Knorr, W.: Global data set of biogenic VOC emissions calculated by the MEGAN
867 model over the last 30 years, *Atmos. Chem. Phys.*, 14, 9317-9341, 10.5194/acp-14-9317-2014,
868 2014.

869 Sindelarova, K., Markova, J., Simpson, D., Huszar, P., Karlicky, J., Darras, S., and Granier, C.:
870 Copernicus Atmosphere Monitoring Service Global Biogenic VOC emissions version 3.1
871 (CAMSGLOB-BIOv3.1), Copernicus Atmosphere Monitoring Service, ECCAD,
872 <https://doi.org/10.24380/cv4p-5f79>, 2021.

873 Stavrou, T., Müller, J. F., Bauwens, M., De Smedt, I., Van Roozendaal, M., and Guenther, A.:
874 Impact of Short-Term Climate Variability on Volatile Organic Compounds Emissions Assessed
875 Using OMI Satellite Formaldehyde Observations, *Geophysical Research Letters*, 45, 8681-8689,
876 <https://doi.org/10.1029/2018GL078676>, 2018.

877 Sun, S., Palmer, P. I., Siddans, R., Kerridge, B. J., Ventress, L., Edtbauer, A., Ringsdorf, A.,
878 Pfannerstill, E. Y., and Williams, J.: Seasonal isoprene emission estimates over tropical South
879 America inferred from satellite observations of isoprene, *EGUsphere*, 2025, 1-28,
880 10.5194/egusphere-2025-778, 2025.

881 Terrenoire, E., Hauglustaine, D. A., Cohen, Y., Cozic, A., Valorso, R., Lefèvre, F., and Matthes, S.:
882 Impact of present and future aircraft NO_x and aerosol emissions on atmospheric composition and
883 associated direct radiative forcing of climate, *Atmos. Chem. Phys.*, 22, 11987-12023, 10.5194/acp-
884 22-11987-2022, 2022.

885 Tiedtke, M.: A Comprehensive Mass Flux Scheme for Cumulus Parameterization in Large-Scale
886 Models, *Monthly Weather Review*, 117, 1779-1800, [https://doi.org/10.1175/1520-0493\(1989\)117<1779:ACMFSF>2.0.CO;2](https://doi.org/10.1175/1520-0493(1989)117<1779:ACMFSF>2.0.CO;2), 1989.

888 Unger, N.: Isoprene emission variability through the twentieth century, *Journal of Geophysical Research: Atmospheres*, 118, 13,606-613,613, <https://doi.org/10.1002/2013JD020978>, 2013.

890 Valin, L. C., Fiore, A. M., Chance, K., and González Abad, G.: The role of OH production in
891 interpreting the variability of CH₂O columns in the southeast U.S, *Journal of Geophysical Research: Atmospheres*, 121, 478-493, <https://doi.org/10.1002/2015JD024012>, 2016.

893 van der Werf, G. R., Randerson, J. T., Giglio, L., van Leeuwen, T. T., Chen, Y., Rogers, B. M., Mu, M.,
894 van Marle, M. J. E., Morton, D. C., Collatz, G. J., et al.: Global fire emissions estimates during 1997–
895 2016, *Earth Syst. Sci. Data*, 9, 697-720, 10.5194/essd-9-697-2017, 2017.

896 Wang, H., Liu, X., Wu, C., and Lin, G.: Regional to global distributions, trends, and drivers of
897 biogenic volatile organic compound emission from 2001 to 2020, *Atmos. Chem. Phys.*, 24, 3309-
898 3328, 10.5194/acp-24-3309-2024, 2024a.

899 Wang, H., Nagalingam, S., Welch, A. M., Leong, C., Czimczik, C. I., and Guenther, A. B.: Heat waves
900 may trigger unexpected surge in aerosol and ozone precursor emissions from sedges in urban
901 landscapes, *Proceedings of the National Academy of Sciences*, 121, e2412817121,
902 doi:10.1073/pnas.2412817121, 2024b.

903 Wang, H., Welch, A., Nagalingam, S., Leong, C., Kittitanuvong, P., Barsanti, K. C., Sheesley, R. J.,
904 Czimczik, C. I., and Guenther, A. B.: Arctic Heatwaves Could Significantly Influence the Isoprene
905 Emissions From Shrubs, *Geophysical Research Letters*, 51, e2023GL107599,
906 <https://doi.org/10.1029/2023GL107599>, 2024c.

907 Wang, H., Welch, A. M., Nagalingam, S., Leong, C., Czimczik, C. I., Tang, J., Seco, R., Rinnan, R.,
908 Vettikkat, L., Schobesberger, S., et al.: High temperature sensitivity of Arctic isoprene emissions
909 explained by sedges, *Nature Communications*, 15, 6144, 10.1038/s41467-024-49960-0, 2024d.

910 Weber, J., King, J. A., Sindelarova, K., and Val Martin, M.: Updated isoprene and terpene emission
911 factors for the Interactive BVOC (iBVOC) emission scheme in the United Kingdom Earth System
912 Model (UKESM1.0), *Geosci. Model Dev.*, 16, 3083-3101, 10.5194/gmd-16-3083-2023, 2023.

913 Wells, K. C., Millet, D. B., Payne, V. H., Deventer, M. J., Bates, K. H., de Gouw, J. A., Graus, M.,
914 Warneke, C., Wisthaler, A., and Fuentes, J. D.: Satellite isoprene retrievals constrain emissions and
915 atmospheric oxidation, *Nature*, 585, 225-233, 10.1038/s41586-020-2664-3, 2020.

916 Wells, K. C., Millet, D. B., Payne, V. H., Vigouroux, C., Aquino, C. A. B., De Mazière, M., de Gouw, J.
917 A., Graus, M., Kurosu, T., Warneke, C., et al.: Next-Generation Isoprene Measurements From
918 Space: Detecting Daily Variability at High Resolution, *Journal of Geophysical Research: Atmospheres*, 127, e2021JD036181, <https://doi.org/10.1029/2021JD036181>, 2022.

920 Wennberg, P. O., Bates, K. H., Crounse, J. D., Dodson, L. G., McVay, R. C., Mertens, L. A., Nguyen,
921 T. B., Praske, E., Schwantes, R. H., Smarte, M. D., et al.: Gas-Phase Reactions of Isoprene and Its
922 Major Oxidation Products, *Chemical Reviews*, 118, 3337-3390, 10.1021/acs.chemrev.7b00439,
923 2018.

924 Wolfe, G. M., Kaiser, J., Hanisco, T. F., Keutsch, F. N., de Gouw, J. A., Gilman, J. B., Graus, M., Hatch,
925 C. D., Holloway, J., Horowitz, L. W., et al.: Formaldehyde production from isoprene oxidation
926 across NO_x regimes, *Atmos. Chem. Phys.*, 16, 2597-2610, 10.5194/acp-16-2597-2016, 2016.

927 Xu, Z. N., Nie, W., Liu, Y. L., Sun, P., Huang, D. D., Yan, C., Krechmer, J., Ye, P. L., Xu, Z., Qi, X. M.,
928 et al.: Multifunctional Products of Isoprene Oxidation in Polluted Atmosphere and Their
929 Contribution to SOA, *Geophysical Research Letters*, 48, e2020GL089276,
930 <https://doi.org/10.1029/2020GL089276>, 2021.

931 Yoon, J. Y. S., Wells, K. C., Millet, D. B., Swann, A. S., Thornton, J. A., Turner, A. J.: Impacts of
932 interannual isoprene variations on methane lifetimes and trends, *Geophysical Research Letters*,
933 in press, 2025.
934 Zhao, Y., Zheng, B., Saunio, M., Ciais, P., Hegglin, M. I., Lu, S., Li, Y., and Bousquet, P.: Air pollution
935 modulates trends and variability of the global methane budget, *Nature*, 10.1038/s41586-025-
936 09004-z, 2025.
937 Zheng, B., Ciais, P., Chevallier, F., Yang, H., Canadell, J. G., Chen, Y., van der Velde, I. R., Aben, I.,
938 Chuvieco, E., Davis, S. J., et al.: Record-high CO₂ emissions from boreal fires in 2021, *Science*, 379,
939 912-917, doi:10.1126/science.ade0805, 2023.

940